The Astrophysical Journal, 626:128–144, 2005 June 10

A COMPREHENSIVE MODEL FOR THE MONOCEROS TIDAL STREAM

J. Peñarrubia,[1] D. Martínez-Delgado,[1] H. W. Rix,[1] M. A Gómez-Flechoso,[2] J. Munn,[3] H. Newberg,[4] E. F. Bell,[1] B. Yanny,[5] D. Zucker,[1] and E. K. Grebel[6]

Received 2004 October 19; accepted 2005 February 3

ABSTRACT

We have compiled an extensive data set on potential parts of the Monoceros tidal stream and performed an exhaustive survey of dwarf galaxy semianalytic orbits in order to constrain its orbital properties. The best-fit orbits are subsequently realized as self-consistent *N*-body simulations in order to reproduce the spatial and velocity distribution of satellite debris. We find that all kinematic and geometric constraints can be fit by a single stream allowing for multiple wraps. The orbital eccentricity and inclination of the progenitor are strongly constrained to be $e = 0.10 \pm 0.05$ and $i = 25^\circ \pm 5^\circ$. Ten new estimates of proper motions from the Sloan Digital Sky Survey clearly exclude all retrograde orbits. Particles lost by the satellite populate two nearly concentric rings, naturally explaining the detection of stream stars at both 6–8 kpc (Ibata et al.; Newberg et al.) and 12–18 kpc (the Tri/And stream; Rocha-Pinto et al.) from the Sun. We have attempted to predict the present location of the Monoceros stream progenitor using different information: (1) the kinematical and spatial distribution of detections, and (2) the different mean metallicity in the inner and the outer rings. Because of the lack of observational data in the whole range of Galactic latitudes, the geometrical/kinematical constraints lead to a wide range of possible locations. By associating older parts of the model stream with lower metallicity parts of the observed data, we argue in favor of a current location of $l \sim 245^\circ$, $b \sim -18^\circ$, with a distance to the Sun $r_s \simeq 15$ kpc. The mass of the progenitor has been poorly constrained because of the slow orbital decay. Similar fits have been obtained for masses $(3-9) \times 10^8\ M_\odot$. We have analyzed the possible common origin of the Canis Major dwarf and the Monoceros stream. The Canis Major dwarf moves on a prograde, nearly circular orbit ($e \simeq 0.16$) in the Milky Way disk ($i \simeq 4^{+14}_{-4}$ deg). This orbital inclination is too low to account for the large vertical dispersion of stream stars. However, the bimodal distribution of radial velocities in the central region found by Martin et al. probably indicates that their selection criteria for identifying dwarf stars lead to a contamination of background stars. In that case, the kinematical data outlined above might result in an underestimate of the orbital inclination. Finally, the distance estimation to Canis Major dwarf is around a factor of 2 smaller than that obtained from our model. Unfortunately, the possible identification of the Monoceros stream progenitor in Canis Major remains unclear.

Subject headings: galaxies: evolution — galaxies: formation — galaxies: halos — galaxies: structure

Online material: color figures

1. INTRODUCTION

In a ΛCDM universe, the inner regions of massive galaxies like the Milky Way gain a large fraction of their mass through tidal disruption and accretion of a large number of low-mass fragments (e.g., van den Bosch et al. 2004). The fossil records of these merging processes may be observable nowadays in the form of long tidal streams or large-scale stellar substructures around the parent spiral galaxies. Numerical galaxy formation simulations show that dynamical friction brings substructures from outer halo regions to the neighborhood of the parent galaxies' disks. If halos are flattened (oblate) and their axisymmetry plane is that of the disk, orbits of nonpolar satellite galaxies tend to become coplanar and circularize with time (Peñarrubia et al. 2004). In this scenario, the tidal debris of several disrupted satellite galaxies might have contributed to the formation of the stellar disk if they followed nearly circular orbits with a low orbital inclination at late times of their evolution (Navarro 2004 and references therein).

The Milky Way is an important laboratory in which the predictions of this cosmological scenario can be tested. In the last decade, large-scale surveys have proved the existence of tidal streams (Sagittarius [Ibata et al. 1994] and Monoceros [Newberg et al. 2002]) in our Galaxy, providing strong observational evidence that disruption of dwarf satellites contributes to the assembly of some components of our Galaxy. These tidal streams offer a unique opportunity to study accretion events in considerable detail using the chemical, kinematic, and spatial distribution of tidal stream's stars, which can be directly compared against predictions of *N*-body simulations of merging events (e.g., Law et al. 2005).

Recently, the Sloan Digitized Sky Survey (SDSS) team reported the discovery of a coherent ringlike structure at low Galactic latitude spanning about 100° in the sky (Newberg et al. 2002; Yanny et al. 2003). Follow-up observations (Ibata et al. 2003) found that this structure of low-metallicity stars surrounds the Galactic disk at Galactocentric distances from ∼15 to ∼20 kpc. Different scenarios have been proposed to explain the nature of this feature in the outer Galactic disk (see Helmi et al. 2003): (1) a new tidal stream (Yanny et al. 2003; Ibata et al. 2003), and (2) a stellar ring resulting from perturbations in the disk similar

[1] Max-Planck-Institut für Astronomie, Königstuhl 17, Heidelberg, D-69117, Germany; jorpega@mpia.de.
[2] Universidad Europea de Madrid, Villaviciosa de Odón, E-28670, Spain.
[3] US Naval Observatory, Flagstaff Station, P.O. Box 1149, Flagstaff, AZ 86002.
[4] Department of Physics and Astronomy, Rensselaer Polytechnical Institute, Troy, NY 12180.
[5] Fermi National Accelerator Laboratory, Batavia, IL 60510.
[6] University of Basel, Venusstrasse 7, Binningen CH-4102, Switzerland.

TABLE 1
OBSERVATIONAL CONSTRAINTS

Authors	*l*-*b* Range (deg)	Type	v_r[a]	μ[b]	N[c]	Symbol
Yanny et al. (2003)	[182, 225], [+28, −27]	CMD	Yes	No	4	Filled triangle
Ibata et al. (2003)	[122, 218], [+30,−25]	CMD[d]	No	No	14	Open triangle
Crane et al. (2003)	[157, 242], [+ 38, −15]	M giant	Yes	Yes[e]	58	Filled triangle
H. J. Newberg et al. (2005, in preparation)	[110, 225], [+ 37, −32]	CMD[d]	No	No	22	Open square
Rocha-Pinto et al. (2003)	[117, 157], [+ 38, −25]	M giant[f]	Yes	No	31	Filled square

[a] Radial velocity measurements.
[b] Proper-motion measurements.
[c] Number of detections.
[d] Possible confusion with thick-disk stars (see § 5.4).
[e] Only for 10 stars.
[f] Tri/And stream.

to the remnants of ancient warps (Ibata et al. 2003). Tracing this structure with Two Micron All Sky Survey (2MASS) M-giant stars, Rocha-Pinto et al. (2003) concluded that its structural characteristics are consistent with an interpretation of this structure as the fossil of a merging dwarf galaxy, similar to the Sagittarius dwarf galaxy (Ibata et al. 1994), in the Galactic plane. Interestingly, Frinchaboy et al. (2004) and Crane et al. (2003) also suggested some nearby Galactic open and globular clusters with coordinated heliocentric radial velocities, indicating a possible common origin with the tidal stream.

Unlike the Sagittarius dwarf galaxy, the Monoceros stream has been detected prior to locating the main body of the parent galaxy. The location is still controversial. From the analysis of the 2MASS catalog, Martin et al. (2004a) reported a strong elliptical-shaped stellar overdensity in the constellation of Canis Major, which is coincident in position and radial velocity with a small group of four globular clusters (see § 5.3). Using a fairly simple model, they identify the CMa overdensity as the main body of the progenitor dwarf galaxy of the Monoceros stream (named the CMa dwarf). Bellazzini et al. (2004) presented color-magnitude diagrams in the surroundings of the CMa location, concluding that the system is situated at 8 ± 1 kpc from the Sun and that it is composed of a metal-rich, intermediate-age population. Momany et al. (2004), however, comparing proper motions and radial velocities of CMa M-giant stars, obtain that the overdensity in this region mimics the thick-disk kinematics. Moreover, they find that the star counts in that region are those expected in the standard Milky Way model if one takes into account the warp and flare of the disk. However, a deep color-magnitude diagram of the center of the CMa overdensity by Martínez-Delgado et al. (2004) shows a very well-defined main sequence consistent with a limited extent in distance, confirming that this stellar population is associated with a distinct, possibly still bound stellar system with properties (surface brightness, absolute magnitude, stellar content) compatible with those of Local group dwarf spheroidal galaxies. On the basis of these last results, the CMa overdensity will be referred to the CMa dwarf galaxy in this work.

In this paper we present the results of an extensive search of possible disruption scenarios of satellite galaxies to explore (1) how many of the "overdensity signatures" can be attributed to a single stream and (2) to constrain its progenitor orbit. With an objective criterion we select those orbits that reproduce the spatial and kinematical distribution of candidate debris. Beyond exploring the possible progenitor location, the results will (1) help to carry out new surveys in different regions of the sky and (2) constrain the thick-disk formation history through the distribution evolution of stripped stars.

This paper has been organized as follows. In § 2 we compile the observational data available so far. Section 3 outlines the galaxy and satellite models that we use in our investigation. We also describe our semianalytic orbit algorithm and the results of the orbital parameter survey. We obtain the distribution of debris via the *N*-body algorithm sketched in § 3.4. In § 4 we compare the best-fit orbit with the observational data, and in § 5 we comment on different implications of our results.

2. OBSERVATIONAL DATA

For the present work, we have attempted a comprehensive compilation of observational constraints on the geometry and kinematics of the Monoceros stream. Given the great deal of activity directed toward detecting tidal streams in general, the diversity of available data sets, and in particular the great interest in the Monoceros stream spawned by the original discovery, the constraints are both numerous and inhomogeneous.

Typically, detections of overdensities have resulted from photometry, finding an excess of main-sequence stars or M giants at a given apparent magnitude. Depending on the tracer population, this approach provides distance estimates of differing quality. Radial velocities are available for a subset of stars within a subset of directions with detected overdensities. In principle, the chemical composition of stars can also serve as a constraint, as it can be expected to vary continuously along the stream, presumably with decreasing metallicity in the most loosely bound (and hence first lost) material. Finally, proper motions (which typically can be measured to $\Delta\mu \sim 3$–4 mas yr^{-1}) can provide some rough constraints; their precision in physical units is, however, only $\Delta v_{\rm perp} = \Delta\mu \times r_s \times 4.74$, where r_s is the distance from the Sun and 4.74 is the factor that converts (kpc mas yr^{-1}) into (km s^{-1}).

We have compiled both published constraints and those available to us but still in the process of publication. A few constraints were derived specifically for the present paper. We have summarized the constraints, their nature (photometric, kinematic, etc.), and their sources in Table 1. In the following plots we use different symbols to distinguish between different data sources. In order to simplify our figures we have made an exception for those data with available radial velocities, which we have been plotted everywhere with filled triangles.

In addition, we have proper motions of confirmed stream star members selected from the radial velocity compilation by Crane et al. (2003). Proper motions are determined by combining recalibrated USNO-B1.0 positions (Monet et al. 2003) with

TABLE 2
PROPER MOTIONS OF MONOCEROS STREAM STARS

l (deg)	b (deg)	r_s (kpc)	v_r (km s^{-1})	μ_l (mas yr^{-1})	μ_b (mas yr^{-1})
186.382.....	23.910	11.2	-6.8 ± 3.9	2.6	-1.9
189.316.....	23.251	12.6	149.4 ± 5.6	0.6	-4.4
186.894.....	24.181	10.0	5.4 ± 3.7	-5.5	-13.9
189.741.....	23.345	12.7	0.2 ± 6.0	6.0	-1.0
198.778.....	25.063	11.9	49.1 ± 2.5	-1.2	2.6
224.108.....	21.344	10.9	82.8 ± 3.4	1.0	-6.3
178.371.....	36.786	10.4	-19.7 ± 2.0	6.1	1.5
186.992.....	38.816	12.3	42.3 ± 2.1	0.4	3.0
221.989.....	29.900	12.3	86.1 ± 3.2	-3.3	-6.2
223.126.....	32.262	11.8	55.1 ± 2.7	-3.5	1.9

NOTES.—Positions in Galactic coordinates of the Monoceros stream stars with measured proper motions. The errors in the heliocentric distance r_s are about 25% of the value, whereas for μ_l and μ_b they have been estimated to be 3.5 mas yr^{-1}.

those from the SDSS[7] catalog, as detailed in Munn et al. (2004). The proper motions of our target stars are given in Table 2. It is necessary to clarify that the measurements of proper motions have not been included in the orbital fit and will be used only to discriminate the sense of motion of the progenitor's orbit.

In addition, we are faced with the problem of which constraints (and on which candidate sections of the Monoceros stream) to include in our modeling. Guided by the goal of finding the largest number of stream portions that may have arisen from a single disruption event, we have used an iterative procedure. Starting with the original stream detections (Newberg et al. 2002; Yanny et al. 2003) and the comprehensive kinematic survey of M stars (Crane et al. 2003) spanning 100° in the sky. Initial modeling of these constraints made it clear that other, independently found overdensities are most likely also part of the stream. In particular, the Tri/And stream (Majewski et al. 2004), a more distant metal-poor stellar stream, showed a location in the sky and a radial velocity curve fairly similar to the predictions of our first-iteration model. Therefore, the available data (including radial velocities from Rocha-Pinto et al. 2003) on the Tri/And stream were then included as inputs in a second iteration of our survey of the best-candidate orbit to better constrain its properties and reduce the number of possible scenarios.

Finally, we explicitly test whether the CMa dwarf is likely part of the stream, presumably the "parent" of the tidal debris. We do this by omitting CMa in the first modeling and then comparing its orbit with that of our model for a possible Monoceros stream progenitor.

3. FITTING NUMERICAL MODELS TO OBSERVATIONAL DATA

In this section we outline how we perform the orbital analysis of dwarf satellites and the method used to fit numerical orbits to the observational data.

We first describe a Milky Way model that matches the mass distribution of our Galaxy. Subsequently, we discuss the parameter space that we must cover in order to determine the orbital characteristics of a possible Monoceros stream progenitor. Finally, we present the method used to constrain the orbital properties of a possible Monoceros tidal stream progenitor, which can be divided in two steps. (1) Satellite orbits are calculated using a well-tested semianalytic algorithm in order to perform a survey of our large parameter space. Subsequently, the orbit collection has been compared against the observational sample to determine the parameter sets that provide the best fits. (2) Once the orbital constraints are known, we carry out N-body simulations to analyze the spatial and kinematical distribution of debris.

3.1. *Galaxy and Dwarf Satellite Models*

Our dynamical model for the Milky Way follows Hernquist (1993), where (1) the disk is exponential in the radial direction and isothermal in the vertical direction; (2) the bulge is described by a Hernquist model (Hernquist 1990) with spherical symmetry; and (3) the halo follows a flattened, nonsingular isothermal profile with given core and cutoff radius.

For the density distributions of the disk we take

$$\rho_d(R,z) = \frac{M_d}{4\pi R_d^2 z_0} \exp(-R/R_d)\mathrm{sech}^2(z/z_0), \quad (1)$$

where $M_d = 5.60 \times 10^{10}\ M_\odot$ is the disk mass, $z_0 = 0.70$ kpc is the vertical thickness, and $R_d = 3.50$ kpc is the exponential scale length in the radial direction. The mass profile decays exponentially with R and is composed of isothermal sheets along the vertical direction. Velocities are assumed to have a Gaussian distribution.

For the bulge we adopt the spherical Hernquist profile (Hernquist 1990),

$$\rho_b = \frac{M_b}{2\pi} \frac{a}{r(r+a)^3}, \quad (2)$$

where $M_b = 1.86 \times 10^{10}\ M_\odot$ is the bulge mass and $a = 0.53$ kpc is the spherical scale length. This analytical profile fits the de Vaucouleurs law (de Vaucouleurs 1948). The velocity field is constructed from the Jeans equations by assuming isotropic Gaussian velocity distributions at each radial distance (Hernquist 1993).

We use a nonsingular isothermal profile for the dark matter halo (DMH),

$$\rho_h = \frac{M_h \alpha}{2\pi^{3/2} r_{\rm cut}} \frac{\exp(-m^2/r_{\rm cut}^2)}{m^2 + \gamma^2}, \quad (3)$$

where

$$m^2 \equiv R^2 + z^2/q_h^2 \quad (4)$$

in cylindrical coordinates; q_h is the halo density flattening, $M_h = 7.84 \times 10^{11}\ M_\odot$ is the DMH mass, $r_{\rm cut} = 84.00$ kpc the cutoff radius, $\gamma = 3.50$ kpc the core radius, and

$$\alpha \equiv \{1 - \sqrt{\pi}\beta \exp(\beta^2)[1 - \mathrm{erf}(\beta)]\}^{-1} = 1 + \sqrt{\pi}\beta + (\pi - 2)\beta^2 + O(\beta^3), \quad (5)$$

where $\beta = \gamma/r_{\rm cut} \lesssim 1/24$ in our calculations. To construct the flattened (oblate) DMHs, a nonhomologous transformation is applied to equation (3) to achieve the desired axis ratio q_h while preserving the central density. In order to minimize computational time when constructing flattened DMHs with embedded

[7] SDSS (York et al. 2000) is an imaging and spectroscopic survey that will eventually cover $\sim\frac{1}{4}$ of the sky. Drift-scan imaging in the five SDSS bandpasses (u, g, r, i, z) (Fukugita et al. 1996; Gunn et al. 1998; Hogg et al. 2001) is processed through data reduction pipelines to measure photometric and astrometric properties (Stoughton et al. 2002; Smith et al. 2002; Pier et al. 2003; Abazajian et al. 2003) and to identify targets for spectroscopic follow-up.

TABLE 3
PARAMETER SPACE

PARAMETER	*l*-*b* RANGE (deg)	PRECISION	NO. OF VALUES	BEST FITS: PROGRADE *pro1*	*pro2*	*pro3*	BEST FITS: RETROGRADE *ret1*	*ret2*	*ret3*
M_s ($\times 10^8\ M_\odot$)	[0.6, 12.0]	± 3.0	3	6.3	6.3	6.3	12.0	12.0	12.0
r_a (kpc).....	[17.5, 80.5]	± 3.5	10	22.8	22.8	22.8	22.8	22.8	22.8
e.....	[0, 0.7]	± 0.05	7	0.1	0.1	0.1	0.5	0.5	0.5
i (deg).....	[5.0, 45.0], [135.0, 175.0]	± 5.0	10	25.0	25.0	25.0	165.0	155.0	165
ϕ (deg)	[0.0, 360.0]	± 15	12	300	150.0	120.0	180	210	210
q_h	[0.0, 360.0]	± 0.05	6	0.6	0.7	0.8	0.6	0.6	0.5
$\chi_{\rm best}$	6.3	...	...	1.92	1.96	1.97	2.34	2.39	2.39

NOTE.—All quantities are given at $t = 0$ of the simulation; r_a denotes the initial distance to the Galaxy center; $e \equiv (r_a - r_p)/(r_a + r_p)$ is the orbital eccentricity; r_a and r_p are the apo- and pericenter distances, respectively; i is the inclination with respect to the disk plane; ϕ is the azimuthal angle in spherical coordinates; and q_h is the axis ratio of the halo's density profile. Values of free parameters are equally distributed with the ranges. Our notation is so that $0^\circ < i < 90^\circ$ indicates a prograde motion, whereas $90^\circ < i < 180^\circ$ a retrograde one.

bulges and disks, we apply a highly efficient technique using multipole potential expansions to tailor the local velocity ellipsoid to the required morphology (Boily et al. 2001). The algorithm to add together individual components in a single galaxy is adapted from Hernquist (1993). This code scales linearly with particle number and hence we can construct flattened DMHs with $\gtrsim 10^6$ particles in a short computational time.

The specific parameters are chosen to reproduce the observed rotational curve of the Milky Way. The only free parameter of the Galaxy model that we explore in our calculations is the halo axis ratio (q_h).

The dwarf satellite model follows a King profile (King 1966) with central potential $\Psi/\sigma^2 = 4$ and concentration $c = \log_{10}(r_t/r_{\rm K}) = 0.84$, where r_t and $r_{\rm K}$ are the tidal and King radii, respectively. Since we are assuming that the tidal debris represent multiple wraps (and thus, multiple perigalacticon passages) of the tidal stream originating from one disrupting satellite, we restrict the tidal radius of the progenitor dwarf galaxy in each model with the following criteria: (1) the tidal radius must be small enough to prevent galaxy disruption by the first perigalacticon passage, and (2) the tidal radius must be large enough to induce a progressive mass loss that leads to the formation of a tidal stream. We have selected the satellite tidal radius to match the Jacobi limit (§ 7.3 of Binney & Tremaine 1987) at the first perigalacticon, which is a simple method to achieve "slow" mass loss along the orbit.

3.2. *Orbital Parameters*

Given the Milky Way and satellite mass profiles, three aspects determine the subsequent orbit evolution: (1) the flattening of the Milky Way halo q_h; (2) the mass of the satellite, determining the degree of dynamical friction; and (3) the initial orbital geometry. The corresponding free parameters are outlined in Table 3. We have performed 151,200 simulations by means of our semianalytic code (see below) in order to fit the observational data. Each orbit is repeated with 12 different azimuthal angles since, a priori, we do not know whether dynamical friction affects the orbit within one orbital period (which would "break" the axisymmetry of the problem).

Because of the high efficiency of the semianalytic code, the resolution achieved in the parameter space is constrained by the limited number of available observational data rather than by CPU limitations. More densely sampled parameter surveys would not provide stronger constraints, owing to the large degeneracy seen already in this sparse sampling of parameters space (see § 4.1).

3.3. *Semianalytic Fit*

Exploring a large number of initial conditions and accounting for the time-dependent dynamical friction and satellite disruption can only be carried out in a reasonable time by using semianalytic algorithms. We have used that proposed by Peñarrubia (2003), which provides, for the galaxy density profile outlined in § 3.1, the evolution of $\boldsymbol{r}$, where $\boldsymbol{r}$ is the satellite center-of-mass position, and the dwarf satellite mass M_s. This code has been tested against N-body calculations for a large spectrum of orbital parameters and satellite masses (Just & Peñarrubia 2005), as well as halo flattenings (Peñarrubia et al. 2004), showing that $|\boldsymbol{r}_{\rm analytic} - \boldsymbol{r}_{N\text{-body}}| \leq 0.7$ kpc for time integrations of 3 Gyr, once the Coulomb logarithm is fit to N-body simulations (the best-fit values being $\ln \Lambda_h = 2.1$ for the halo and $\ln \Lambda_d = 0.5$ for the disk).

In order to compare our collection of orbits to the observational data we assume that the distribution of stream stars can be reproduced by a single stream within a given number of wraps. Equivalently, we can define the number of wraps as the time interval that a point-mass particle needs to cover the phase space defined by the observational data, ΔT, which a priori is an unknown quantity that we have estimated from our N-body simulations to lie between $2T_{\rm orb} \leq \Delta T \leq 3T_{\rm orb}$, where $T_{\rm orb} = 2\pi r/v_c$ is one dynamical period at $r \sim 20$ kpc from the Galaxy center; $v_c = 220\ {\rm km\ s^{-1}}$. The maximum integration time of semianalytic orbits is $T_{\rm max} = 5T_{\rm orb} \simeq 3$ Gyr.

The fitting algorithm that we use is the following:

1. Each orbit is divided into n overlapping segments of extension ΔT. Following the above discussion, we carry out the fit for stream extensions of $\Delta T = 1.2$ and 1.8 Gyr (i.e., $\Delta T \simeq 2$ and $3T_{\rm orb}$). The number of segments for a single orbit is $n = 4$ and 3, respectively.[8]
2. For a given segment we calculate

$$\chi^2_{i,j} = \left(\frac{\boldsymbol{r}_{j,\,\rm analytic} - \boldsymbol{r}_{i,\,\rm obs}}{\sigma_{r,\,i}}\right)^2 + \left(\frac{v_{j,\,\rm rad,\,analytic} - v_{i,\,\rm rad,obs}}{\sigma_{v,\,i}}\right)^2,$$

[8] This selection leads to fixed overlapping time intervals of extension $(n\Delta T - T_{\rm max})/(n-1)$, i.e., 0.6 Gyr for $n = 4$ and 1.2 Gyr for $n = 3$.

where $v_{\rm rad}$ is the heliocentric radial velocity and $\sigma_{r,i}$ and $\sigma_{v,i}$ are, respectively, the errors in the distance estimation and in the radial velocity of the observational point i. The distance error is approximately 15% of the heliocentric distance, whereas $\sigma_v \simeq 5$ km s^{-1}. The subindexes i and j take the values $i = 1, 2, \ldots, N_{\rm obs}$, where $N_{\rm obs}$ is the number of observational data, $j = 1, 2, \ldots, N_{\rm analytic}$, and $N_{\rm analytic}$ is the number of semianalytic points in a segment. Subsequently, for each observational value i we look for the semianalytic point that leads to the smallest value of $\chi_{i,j}$, obtaining a set of $N_{\rm obs}$ semianalytic points where the χ-values find a minimum. The average value of χ in a given segment is $\chi = \sum \chi_i / N_{\rm obs}$.

3. The calculation is repeated for the rest of segments.

4. The χ-values of each segment are sorted, obtaining the time interval of the orbit where the best fit occurs and the minimum χ. This method allows us to fit more than one orbital period to observational points located in a small region of the space that were possibly stripped in different orbital wraps (see § 4.2).

5. The process repeats for the whole orbit collection (regarding that each orbit corresponds to one point of our parameter space).

3.4. *N-body Code*

The semianalytic code reproduces remarkably well the motion of a dwarf satellite center of mass and its mass evolution. However, as Piatek & Pryor (1995) showed, the mass-loss process itself is fairly complicated and difficult to implement in semianalytic algorithms.

In order to describe the distribution of stripped stars in the Galaxy we perform N-body simulations from the best-fitting orbits found using the semianalytic code. We carry out self-consistent N-body calculations with SUPERBOX, a particle-mesh code (see Felhauer et al. 2000), which calculates the gravitational potential in three boxes centered at the disk, bulge, halo, and dwarf satellite, each box with 64^3 grid cells. We refer the reader to Peñarrubia (2003) and Peñarrubia et al. (2002) for a detailed description of the code parameters. Here we merely comment that, after fixing the time step to 0.65 Myr, we obtain a conservation of total energy and total angular momentum of around 1%.

The number of particles of each subsystem is $N_d = 9.0 \times 10^4$ (disk), $N_b = 5.0 \times 10^3$ (bulge), $N_h = 1.2 \times 10^6$ (dark matter halo), and $N_s = 1.0 \times 10^5$ (dwarf galaxy).

As in the case of semianalytic calculations, we evolve N-body satellites approximately 3 Gyr. Three aims lead us to select this integration time: (1) to reproduce semianalytic calculations thoroughly; (2) to minimize feedback effects from the host galaxy affecting real dwarf satellites that are difficult to implement in N-body realizations of the Milky Way (such as the disk's spiral arms, overdensity regions, and warps; those effects can be treated like small corrections to our Galaxy potential and thus be neglected in short-time orbit calculations); and (3) to approximate the orbits of tidal stream stars as the orbit of the main system. When obtaining the progenitor's main orbital properties from semianalytic calculations, one assumes implicitly that the escaping particles follow the main system's orbit during a given time interval. This assumption only holds, therefore, for a limited number of orbital periods.

4. RESULTS

4.1. *Semianalytic Solutions*

In Figure 1 we plot the results of our semianalytic fit to observational data for two different stream extensions, $\Delta T \simeq 2T_{\rm orb}$ and $3T_{\rm orb}$, and for prograde and retrograde orbits, as the sense of rotation has not yet been unambiguously determined.[9] This figure shows that the best-fitting parameter values do not depend on the exact value of ΔT. However, larger segments do alter the value of the minima and the smoothness of the curves by increasing the ratio $N/N_{\rm obs}$ (i.e., in a given segment, more semianalytic points can be fit to the same number of observational constraints), improving the quality of the fit but at the same time leading to less pronounced minima, which hardens the selection of the best-fitting parameter sample.

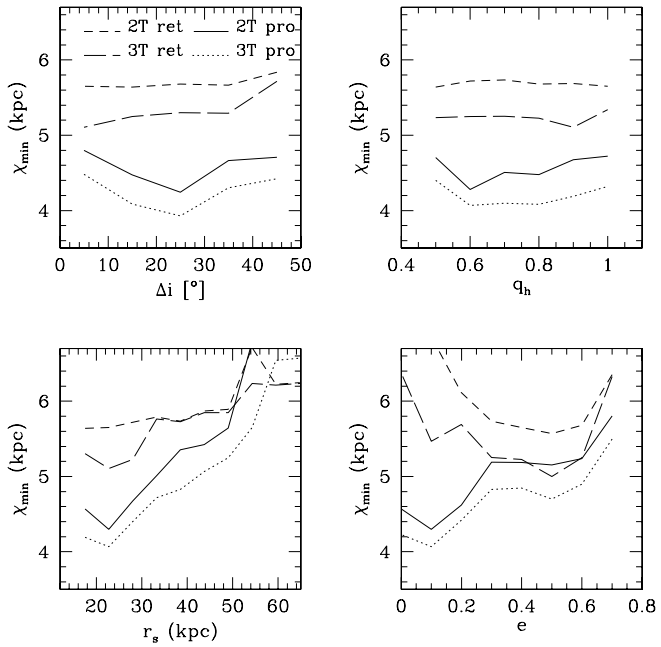

FIG. 1.—Minimum values of the fitting parameter χ as a function of initial heliocentric distance (*bottom left panel*), eccentricity (*bottom right panel*), halo axis ratio (*top right panel*) and orbital inclination (*top left panel*). For each parameter, we perform the fit assuming that the observed tidal stream can be reproduced by an orbit segment of extension $\Delta T \simeq 2T_{\rm orb}$ (*solid lines*) or $3T_{\rm orb}$ (*dotted lines*).

In the bottom right panel we show the minimum value of χ as a function of the orbit's initial eccentricity. The minima are located at $e \simeq 0.1$ for prograde orbits and $e = 0.5$ for retrograde ones. As we see in the bottom left panel, the initial heliocentric distance that leads to best fits independent of the orbital sense of motion is $r_s \simeq 22.8$ kpc.

In the top left panel we show the dependence of $\chi_{\rm min}$ on the inclination angle with respect to the disk plane (note that the orbital inclination of retrograde orbits is $i = 180 - \Delta i$ with this notation). We find that the orbital inclination of retrograde orbits cannot be accurately determined. These orbits reach the solar circle, which therefore reduces the number of passages by the Galactic anticenter (where most of the observational data are located). As a result, retrograde solutions cannot account for the large vertical dispersion of observational points (see Fig. 3). In contrast, prograde orbits present a well-marked minimum at $i \simeq 25^\circ$.

The absence of a defined vertical structure of debris also leads to a degenerate value of the halo flattening, as we see in the top right panel. For prograde orbits, the halo axis ratio that leads to the best solution is for $q_h = 0.6$, although similar $\chi_{\rm min}$ values have been found for $q_h = 0.7$ and 0.8. No information about the halo flattening can be obtained from the fit if orbits are retrograde.

[9] As Martin et al. (2004a) pointed out, the radial velocity curve as a function of projected position does not provide by itself sufficient information to determine whether the progenitor of the Monoceros stream follows a prograde or a retrograde orbit.

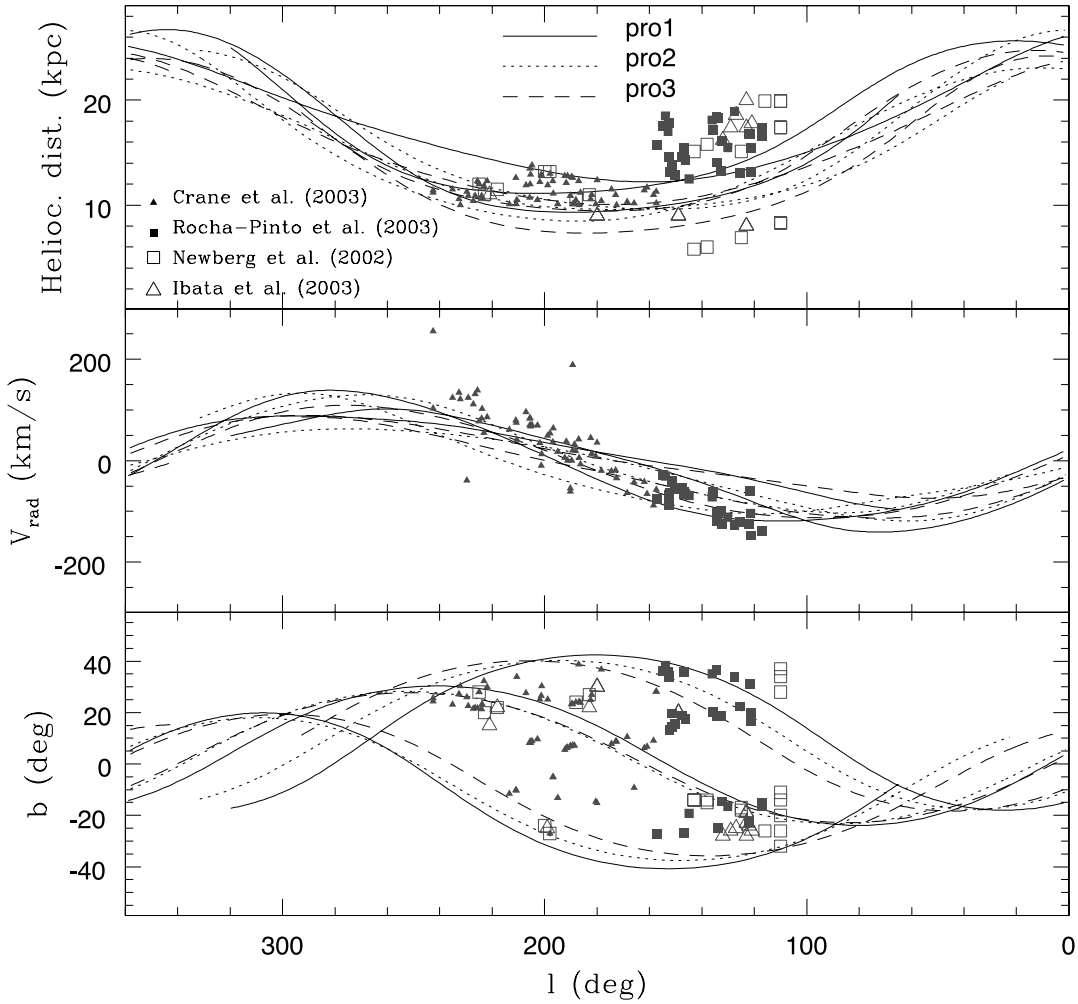

FIG. 2.—Best-fitting prograde solutions (see Table 3). *Top panel:* Heliocentric distance as a function of Galactic longitude (l). *Middle panel:* Heliocentric radial velocity. *Bottom panel:* Projected spatial position in the l-b plane. Open triangles and filled squares represent detections of stars. Open squares denote color-magnitude detections (with no radial velocity measurements available). [*See the electronic edition of the Journal for a color version of this figure.*]

As one would expect, there are a large number of orbits that lead to similar values of χ. That is far from surprising when one takes into account that (1) the region of the Galaxy where the Monoceros stream has been detected is relatively small ($r_s \in [12,\ 20]$ kpc, $110^\circ < l < 240^\circ$, in Galactic coordinates), which represents a small interval of the orbit, and (2) the stream presents a large dispersion in the z-direction (perpendicular to the disk plane) with a poorly defined structure (see Fig. 2).

In Table 3 we summarize the fit results and show the three best-fitting retrograde and prograde orbits. The values of $\chi_{\rm min}$ clearly indicate that retrograde orbits lead to considerably worse fits, $\chi_{\rm ret} \simeq 1.24\chi_{\rm pro}$.

Our fit technique also provides a coarse estimate of the progenitor's initial mass, which we estimate to be around $6 \times 10^8\ M_\odot$ if it moves on a prograde orbit and $1 \times 10^9\ M_\odot$ if the orbit is retrograde. We remark that this result is fairly approximate (see precision estimates in Table 3), since the orbital decay within 3 Gyr is very low for prograde orbits and practically negligible for retrograde ones (note that the effect of the dwarf satellite mass on the semianalytic orbit calculation occurs through dynamical friction). The poor sensitivity of the result to the satellite mass justifies our early choice of a coarse grid in satellite masses.

In Figure 2 we compare the semianalytic satellite orbits with the observational data used for the fit. We only show the orbit at the time interval when the best fit to the observations occurs (see § 3.3). The best prograde orbits stay relatively far from the Galaxy center, $r \in [20,\ 25]$ kpc, and have a pericenter at $l \simeq 180^\circ$. Different values of halo flattening and initial azimuthal angle match the observed heliocentric distances, radial velocities, and projected positions of debris with a similar accuracy, leading to multiply degenerated solutions.

In Figure 3 we illustrate our best-fitting retrograde orbits. Those orbits have an apogalacticon at $l \simeq 180^\circ$, where most of observational points are located. They reach the solar circle, moving within $r \in [7.5,\ 22]$ kpc. Since orbits in the Galactic potential follow rosettes, the retrograde orbits pass the Galactic anticenter considerably less frequently than the prograde ones.

The satellite tidal radius was selected to match that of the Galaxy at the pericenter; therefore, we find that for prograde satellites $(r_{\rm K},\ r_t) = (0.51,\ 1.79)$ kpc whereas for retrograde ones $(r_{\rm K},\ r_t) = (0.08,\ 0.54)$ kpc, where $r_{\rm K}$ and r_t are the King and the tidal radius, respectively. Note that our retrograde satellites are approximately 3.3 times smaller than the progrades in order to prevent tidal disruption by the first perigalacticon passages.

4.2. *N-body Calculations: Orbital Sense of Motion*

In this section we analyze the resulting kinematical and spatial distribution of debris from the best-fitting orbits obtained by our N-body algorithm. In Figure 4 we plot the projection of the pro- and retrograde orbits in the X-Y plane, the radial velocity curve,

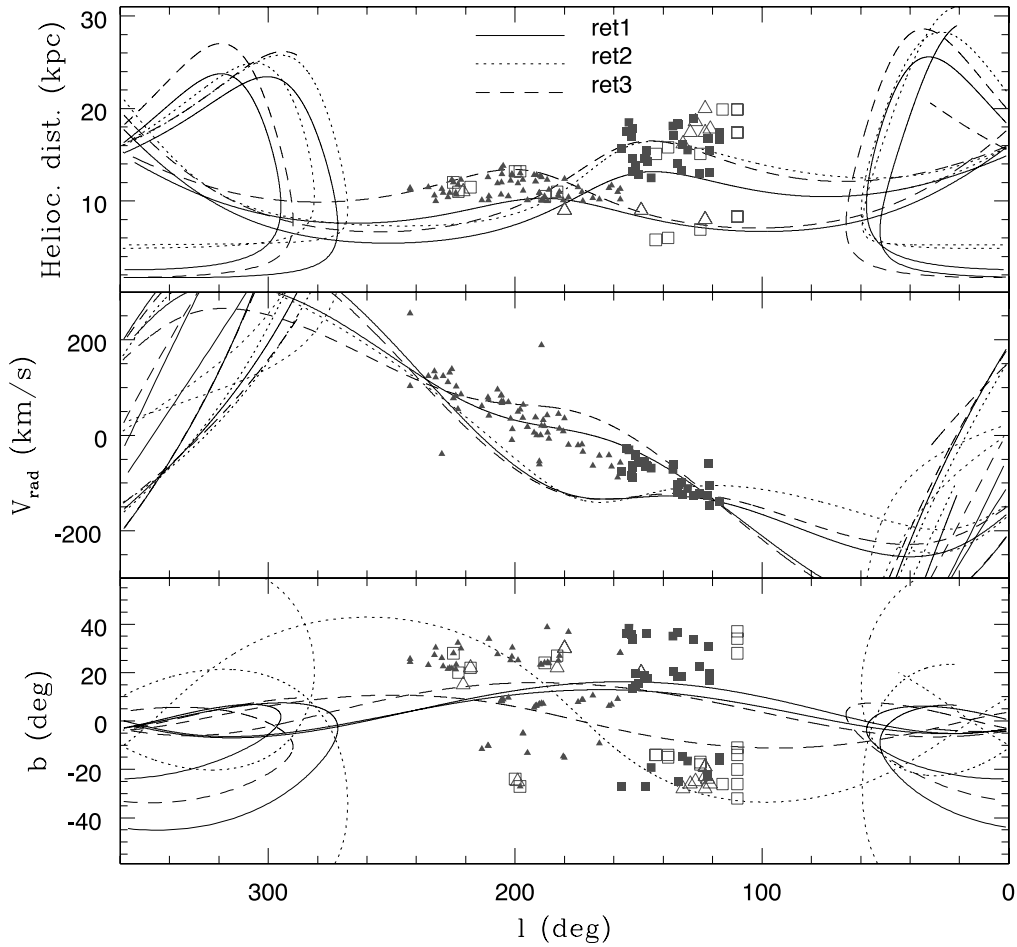

FIG. 3.—Same as Fig. 2, but for our best-fitting retrograde solutions. [*See the electronic edition of the Journal for a color version of this figure.*]

and proper motions (in Galactic longitudinal and latitudinal components) obtained from *N*-body realizations of our best-fit models and compare them to the observational data outlined in § 2. We have integrated the prograde orbit for 2.99 Gyr in order to reproduce the observed projected distribution of debris (see § 4.3), whereas the retrograde one was evolved only 1.9 Gyr, until it was close to total disruption. Even imposing the initial satellite tidal radius to match the Jacobi limit at the first perigalacticon distance (which leads to a retrograde satellite approximately 3.3 times smaller than the prograde one) is not sufficient to assure longer survival times, likely because of the enhanced mass loss induced by disk and bulge tidal shocks.

4.2.1. *Debris Kinematics*

As noted in § 4.1, the slope of the radial velocity curve nearby the Anticenter $dv_{\rm rad}/dl$, $l = 180^\circ$ can be well reproduced either by low eccentricity, prograde orbits with perigalacticon at $l \simeq 180^\circ$ or by high eccentricity, retrograde orbits with apogalacticon at $l \simeq 180^\circ$. Hence, the information provided by the radial velocity curve is not sufficient to determine the rotational sense of motion of the tidal stream progenitor. We must remark on the notably low observational velocity dispersion, which is better reproduced by the prograde model, as one would expect from semianalytical results (see Fig. 2, *middle panel*).

Proper motions in the latitudinal direction do not break the degeneracy between the two different orbital senses of motion either, since both models predict a similar range of μ_b values, consistent with the observations taking into account the large error bars. In contrast, proper-motion constraints in the Galactic plane direction, μ_l, settle the sense of rotation to be prograde (Fig. 4, *right panels, bottom plots*). The prograde model predicts proper motions in that region in the range $\mu_l \in (-5,\ 0)$ mas yr^{-1}, whereas for the retrograde model we find a much larger azimuthal angular velocity $\mu_l \in (5,\ 20)$ mas yr^{-1} due to the larger relative velocity between the Sun and the dwarf galaxy. In order to conclusively differentiate the orbital sense of motion, we use proper motions of 10 stars in the stream derived by Munn et al. (2004). Comparing these measurements with the theoretical predictions we find that, except for two stars, observed values of μ_l are remarkably well reproduced by the prograde model (in magnitude as well as in sign).

We have transformed v_r, μ_l, and μ_b into Cartesian velocities in the Galaxy frame (eq. [7]) in order to determine the components of angular momentum and the orbital inclination $\cos i = -L_z/L$, where $L^2 = L_R^2 + L_z^2$ is the total angular momentum per unit mass.[10] In Figure 5 we plot the distribution of *N*-body particles (models *pro1* and *ret1*) and observational points in the angular momentum plane L_R-L_z (*top panel*). Tidal stream particles are located in well-defined regions determined by the main orbital inclination ($L_z < 0$, $L_z > 0$ for prograde and retrograde orbits, respectively) and by the main eccentricity (which decreases for

[10] We note that the observational values of L_R are positive definite quantities with large errors, which leads to a biased estimate unless some statistical correction is applied. We have corrected them by using the technique of Wardle & Kronenberg (1974).

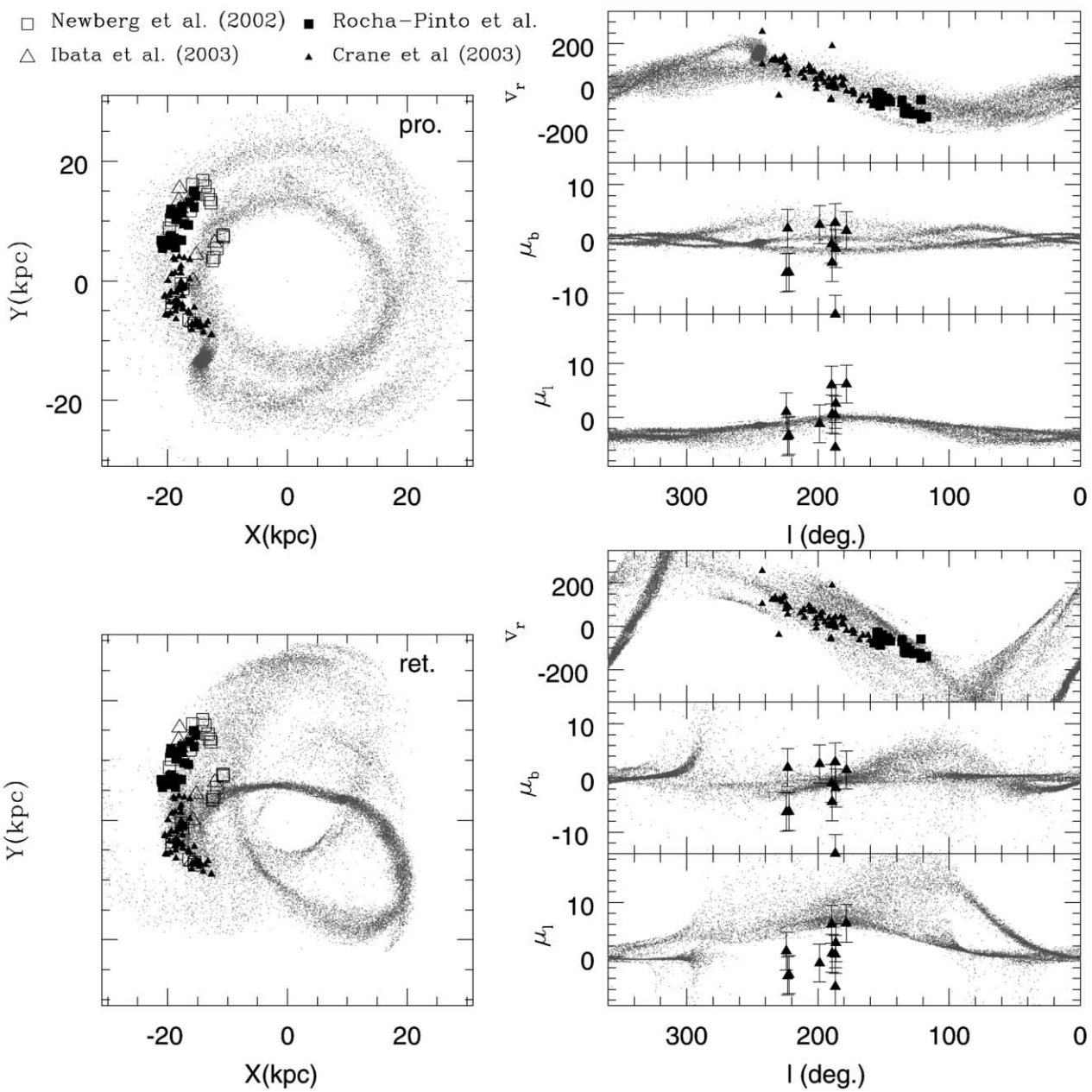

FIG. 4.—Prograde (model *pro1*) vs. retrograde (model *ret1*) orbits. *Left panels: X-Y* Galaxy plane projections. The sun is placed at $(X,\ Y,\ Z) = (-8,\ 0,\ 0)$ kpc. *Right panels:* Heliocentric radial velocity curve (*top plots;* given in km s^{-1}). Proper motions in the latitudinal (*middle plots*) and in the longitudinal (*bottom plots*) components, both given in mas yr^{-1}. [*See the electronic edition of the Journal for a color version of this figure.*]

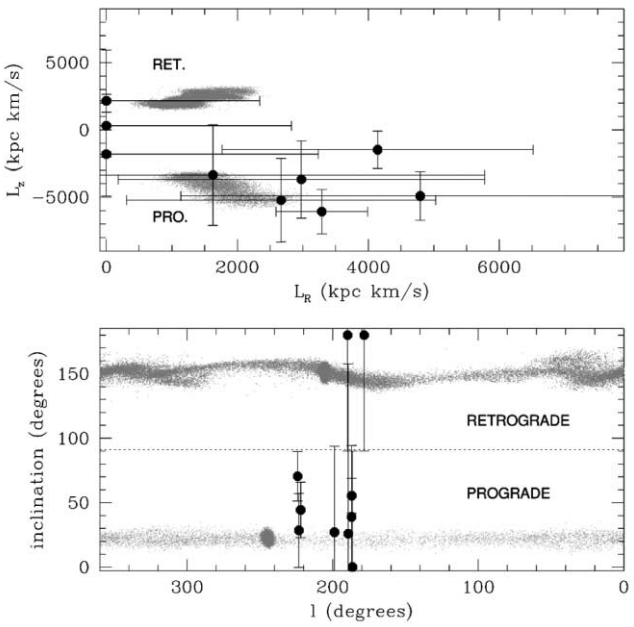

FIG. 5.—*Top panel:* Prograde (model *pro1*) vs. retrograde (model *ret1*) values of the angular momentum components. Dots represent observational values after being corrected (see text). *Bottom panel:* Orbital inclination as a function of Galactic longitude.

decreasing values of L_R). In the bottom panel we plot the orbital inclination as a function of Galactic longitude ($i < 90^\circ$ prograde orbits, $i > 90^\circ$ retrograde orbits), which shows that the Monoceros stream progenitor likely follows a prograde orbit. Unfortunately, the observational errors are too large to provide an estimation of the main orbital inclination from these stars.

It is interesting to note that simply by measuring kinematical properties of stream stars (radial velocities plus proper motions) we would be able to determine not only the sense of motion of the progenitor system, but also its orbital eccentricity and inclination if those measurements were accurate enough.

4.2.2. *Geometrical Distribution of Debris*

As Figure 5 shows, the kinematical properties of tidal stream particles are similar to those of the progenitor during several periods. As a result, the spatial distribution of debris is an approximate representation of the dwarf galaxy orbit. In Figure 4 we show the projection in the Galactic *X*-*Y* plane of dwarf galaxy *N*-body particles for models *pro1* and *ret1*, observing the following:

1. Stripped particles from the prograde satellite are located preferentially at two Galactocentric distances, $r \simeq 12$ and $r \simeq 22$ kpc, building two nearly concentric "rings" in space. That peculiar spacial distribution forms because of (*a*) the low orbital eccentricity and (*b*) the anisotropic mass loss. As Piatek & Pryor (1995) found, disrupting dwarf galaxies become elongated owing to the action of tidal fields. Stripped particles escape preferentially parallel to the major axis, which, at the same time, is oriented perpendicular to the density gradient vector. Because of this process, particles belonging to the trailing and the leading tails move, respectively, outward and inward with respect to the main-body orbit. This process can be clearly seen in the top left panel, the satellite center of density being located at $(X, Y) = (-15, -15)$ kpc and moving clockwise.

2. The retrograde orbit forms a rosette with apogalacticon at 22 kpc and perigalacticon at 7.3 kpc, also providing a reasonably good fit to the Monoceros star detections but failing to reproduce the gap between the two tails observed in the Tri/And regions.

4.3. *Position of the Main Body*

There are some facts that point to the possible survival of the Monoceros stream's progenitor. Stars escaping from a tidally disrupting system follow the main system orbit for some time (the exact evolution of their orbits depend on several parameters), building up what has been defined as "tidal tails." Stars that were lost several orbital periods ago follow orbits in the host galaxy potential nearly independent of their parent system. These particles would spread in a large volume of space (no overdensity signature) with no velocity gradient. Helmi et al. (2003) find that only careful measurements of the phase-space structure might indicate whether they belonged originally to a disrupted body. According to their predictions, the spatial location of debris forming a typical tidal stream structure, as well as their well-defined radial velocity curve, indicates that the tidal tails that we observe are possibly *young* and, therefore, either (1) the main body has not been yet completely destroyed or (2) the disruption occurred recently.

As shown in § 4.1, the range of distances and Galactic latitudes where parts of the stream are detected provides robust values of the orbital inclination and eccentricity of the progenitor. However, the exact vertical and radial distribution of debris depends on the location of the main body (or, equivalently, the time when we stop the *N*-body simulation).

We have two main constraints to fix the progenitor location: (1) geometrical distribution of debris and (2) different metallicities observed in different regions.

Geometrical constraint.—Detections obtained so far show that the Monoceros stream forms a complex vertical structure from the disk plane, if all detections belong to a single tidal stream. In this paper we explore the scenario in which such structure arises from a single disrupted satellite. Different studies (Majewski et al. 2004; H. J. Newberg et al. 2005, in preparation) have reported the presence of two parts of the stream at $l \simeq 110^\circ$, both located at similar projected position but at different heliocentric distances. Observations close to the disk plane do not show the presence of the distant tail ($b \in [-20^\circ, 20^\circ]$), likely because of dust absorption, up to $b > 20^\circ$, where it is again detected. We note that the close tail has been detected only at negative latitudes ($b \in [-20^\circ, -10^\circ]$).

We mainly use observational points at $110^\circ \leq l \leq 130^\circ$ to determine the progenitor position, since the range of distances of detections at $l \in [140^\circ, 240^\circ]$ is considerably smaller, which therefore provides a weaker constraint. Looking at this longitudinal range we observe that if the main body is placed at $l > 100^\circ$ (integration time $t < 2.66$ Gyr), we find no distant tail at $-25^\circ \leq b \leq -20^\circ$ (only leading-tail particles moving in the closest "ring" can be found in this region), whereas if we place the main body at $l < 200^\circ$ (integration time $t > 3.04$ Gyr), we find a luminous close tail at $b > 20^\circ$, not present in observations. Therefore, we obtain comparable fits to observations if the main body is located in the range $100^\circ \geq l \geq 200^\circ$, which corresponds to integration times from 2.66 to 3.04 Gyr, respectively (note that prograde orbits move with $dl/dt < 0$).

Metallicity constraint.—Detections of the distant tail at $100^\circ \leq l \leq 150^\circ$ show metallicities considerably lower than those of the close tail in the same longitudinal range (Rocha-Pinto et al. 2003). Although we have no information on the initial metallicity gradient of the progenitor, we assume that (1) stars with originally high binding energy are those with the highest metallicity, as star

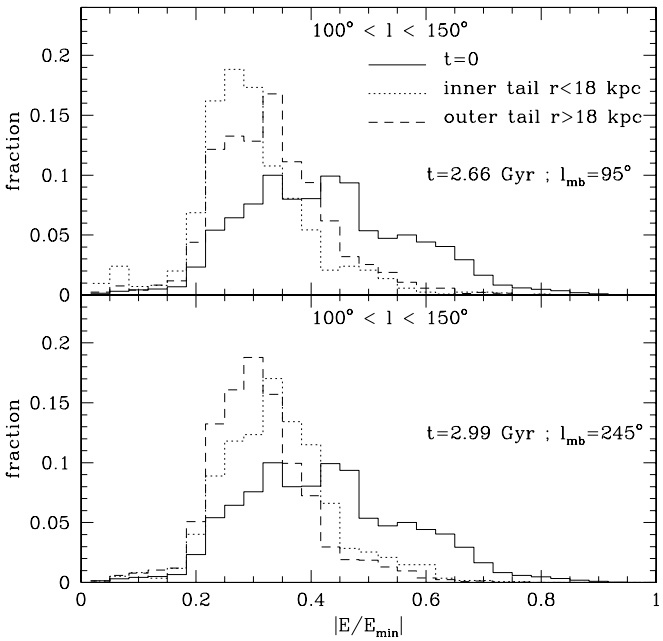

FIG. 6.—Distributions of initial binding energies. We compare the initial distribution (*solid lines*) with that at $t = 2.66$ Gyr (*top panel*) and $t = 2.99$ Gyr (*bottom panel*) for particles in the range $100^\circ \leq l \leq 150^\circ$. For each integration time we distinguish between particles in the "inner ring" ($r < 18$ kpc from the Galaxy center; *dotted lines*) and in the "outer ring" ($r > 18$ kpc; *dashed lines*). At $t = 2.66$ and $t = 2.99$ Gyr the main body is located at $l_{\rm mb} = 95^\circ$ and $l_{\rm mb} = 245^\circ$, respectively. We assume that particles with initial high binding energy $|E/E_{\rm min}| \sim 1$ would present higher metallicities than those with low binding energy at $t = 0$, $|E/E_{\rm min}| \sim 0$.

formation and metallicity enrichment happen more intensely in the center of dwarf galaxies (Pagel & Edmunds 1981; Harbeck et al. 2001) and (2) those processes generating or enhancing any metallicity gradient have stopped, or are very slow, in the last 3 Gyr.[11]

Under those assumptions, the actual distribution of stream metallicities is related to the age of the tidal tails, since low-metallicity stars with low binding energy are stripped out by the action of tidal forces more rapidly than stars with initially high binding energy and high metallicity, which will be preferentially located in recently stripped tails.

Matching the metallicity observed in different regions of the stream reduces the range of possible progenitor locations obtained from geometrical and kinematical constraints. We have compared relative metallicities between the distant and the close tails within $100^\circ \leq l \leq 150^\circ$. In Figure 6 we plot the distribution of stream particles as a function of their initial binding energy for two different positions of the main body (equivalently, two final integration times). Solid lines show the initial distribution (once the satellite is numerically relaxed), and dotted and dashed lines show the distribution of particles with $r < 18$ kpc ("inner ring") and $r > 18$ kpc ("outer ring"), respectively.

The top panel of Figure 6 shows the result of placing the satellite at $l = 95^\circ$. We can see that the number of particles with low initial binding energy (which one would expect to be metal-poor) is larger in the close tail, contradicting observations. If we integrate a longer time, so that the main body locates at $l = 245^\circ$, the number of particles in the distant tail with initial low binding energies is clearly larger than in the close tail. In this case, the outer tail has in average lower metallicity than the close one.

It is interesting to note that the ideal mass-loss process, in which mass shells are progressively removed, is fairly approximate. Shell crossing occurs during the evolution of the satellite, likely because of the action of Galactic tidal forces and shocks. As a result, we observe the presence of particles with initially high binding energy in both stream tails. This fact might explain observations of high- and low-metallicity stars in same fields (e.g., Rocha-Pinto et al. 2003). Although some mixing occurs, Figure 6 shows that the number of particles with initial high binding energy that remain in the main system is larger than in the tidal streams.

In Figure 7 we plot the heliocentric distance (*top panel*) and Galactic latitude (*middle panel*) of debris as a function of Galactic longitude. The bottom panels show the distribution of particles around the main system position. The combination of geometrical and metallicity constraints fixes the main body at $l \sim 245^\circ \pm 3^\circ$, $b \sim -18^\circ \pm 2^\circ$, corresponding to an integration time of $t = 2.99$ Gyr. The heliocentric distance is approximately 15.2 ± 0.8 kpc.

We note that this result is not definitive. Unfortunately, the available data are not yet sufficient to provide strong constraints on the main system location. The progenitor position presented here is fairly approximate and is based on the assumption of an initial metallicity gradient of the progenitor. We expect that future detections, mapping larger areas of the sky, will provide stronger geometrical constraints and reduce the number of possible scenarios.

5. DISCUSSION

In this section we discuss the possible identification of the Monoceros stream progenitor in CMa (Martin et al. 2004a), by comparing its orbital properties to those of our model *pro1*. We also analyze the orbits of three globular clusters with measured proper motions thought to be associated with the CMa dwarf. Finally, we briefly summarize and discuss alternative explanations for the Monoceros tidal stream that can be found in the literature.

5.1. *The Triangulus/Andromeda Stream*

In Figure 8 we show the location of the recent detected Tri/And tidal streams (Rocha-Pinto et al. 2003; *filled squares*) against the debris distribution of model *pro1* (*gray*). We also show those detections used to constrain the orbital parameters. The location and radial velocity of CMa overdensity region is shown by a large open circle. The prograde model suggests the recently discovered stream in Triangulus/Andromeda as natural part of the Monoceros stream, both fitting accurately to the modeled kinematics and spatial distribution of debris. The observed Tri/And streams ($l \in [120^\circ,\ 150^\circ]$) appear as a connection between the Monoceros stream ($l \in [160^\circ,\ 240^\circ]$) and the new SDSS and Ibata detections at $l \in [110^\circ,\ 140^\circ]$, justifying the inclusion of these data in our fit, as we discuss in § 2.

5.2. *The Canis Major Dwarf as the Progenitor of the Monoceros Tidal Stream*

Martin et al. (2004a) identified an elliptical overdensity of M-giant stars in the CMa region with properties suggestive of a disrupted dwarf galaxy: (1) standard models of the Milky way cannot account for the large number of red giants in that region of

[11] This assumption is made in order to compare consistently the initial and the final distribution of binding energies. New episodes of star formation during the tidal disruption of the dwarf galaxy would likely occur in the central regions of the system (thus, increasing the metallicity gradient), which does not alter the conclusions of our comparison.

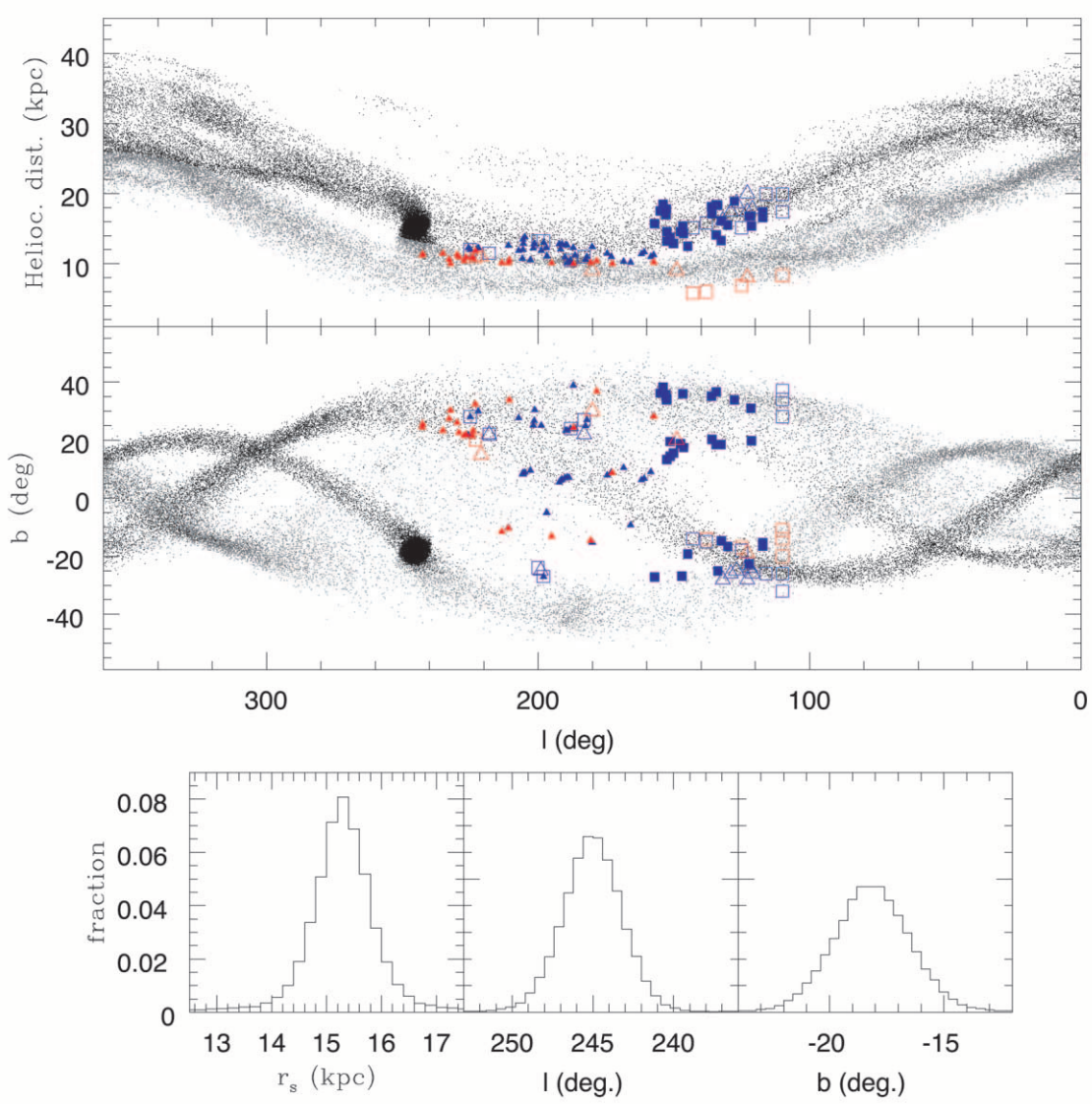

FIG. 7.—Model *pro1* integrated for 2.99 Gyr. Heliocentric distance (*top panel*) and Galactic latitude (*middle panel*) of debris as a function of Galactic longitude. We use notation of Fig. 4 to distinguish different observational sources. Gray and black dots denote, respectively, particles at $r \geq 18$ kpc ("outer ring") and $r < 18$ kpc ("inner ring") from the Galaxy center. The bottom panels show the distribution of debris around the main system remnants. From left to right we plot the heliocentric distance and the Galactic longitude and latitude distributions, which are normalized to the total number of dwarf galaxy stars ($N_s = 10^5$).

our Galaxy, and (2) the low dispersion of the radial velocity distribution (approximately 20-25 km s^{-1}) is unexpected for a disk population. From the number of M-giant stars, these authors estimate a mass of 10^8–10^9 $M_\odot$, similar to the Sagittarius dwarf galaxy. The location in Galactic coordinates is $220^\circ \leq l \leq 260^\circ$, $-15^\circ \leq b \leq -7^\circ$, with no data for $b > -7^\circ$ because of dust absorption. In a second paper, Martin et al. (2004b) find that the heliocentric distance of this systems is $r_s \simeq 7.2 \pm 2$ kpc, with the maximum surface density being located at $l = 240^\circ$ and $b = -8.^\circ 8$. They also measure a the radial velocity of $v_r = 109$ km s^{-1}. Adopting the selection criteria of Bellazzini et al. (2004) and Martin et al. (2004a) to select M-giant stars from the CMa field, Momany et al. (2004) measure the following proper motions $(\mu_l,\ \mu_b) = (-3.5 \pm 2,\ -0.1 \pm 2)$ mas yr^{-1}.

Martin et al. (2004a) concluded that CMa is a satellite galaxy undergoing tidal disruption, and because of its apparent similar position, they suggested that it probably is the remnant of the Monoceros stream progenitor. Here we compare the orbital properties of CMa to our best fit of the Monoceros stream progenitor in order to analyze a possible common origin of both systems. We must remark that our comparison is still fairly preliminary since it goes beyond the original scope of this paper.

5.2.1. *Orbit Calculation*

We have integrated the orbit of CMa back in time in order to compare its kinematical properties with those of our model. The velocity of CMa in Cartesian coordinates with origin in the Galactic center was obtained using the following expression:

$$\begin{aligned}\dot{\boldsymbol{r}} = \dot{\boldsymbol{r}}_\odot &+ v_{\rm rad}(\cos b \cos l,\ \cos b \sin l,\ \sin b)\\ &+ r_s \mu_l \kappa(-\cos b \sin l,\ \cos b \cos l,\ 0)\\ &+ r_s \mu_b \kappa(-\sin b \cos l,\ -\sin b \sin l,\ \cos b), \qquad (6)\end{aligned}$$

where $\dot{\boldsymbol{r}}_\odot = (10.0,\ 225.2,\ 7.2)$ km s^{-1} (Binney & Merrifield 1998) is the solar velocity, r_s the heliocentric distance, and $\kappa \simeq 4.74$ a conversion factor from (kpc mas yr^{-1}) to (km s^{-1}). The velocity vector is $(-145.4,\ 193.2,\ -4.2)$ km s^{-1}. The resulting CMa orbit has low inclination ($i = 4^\circ$) and is nearly circular $e \simeq 0.16$, as argued by Momany et al. (2004). Figure 9 shows

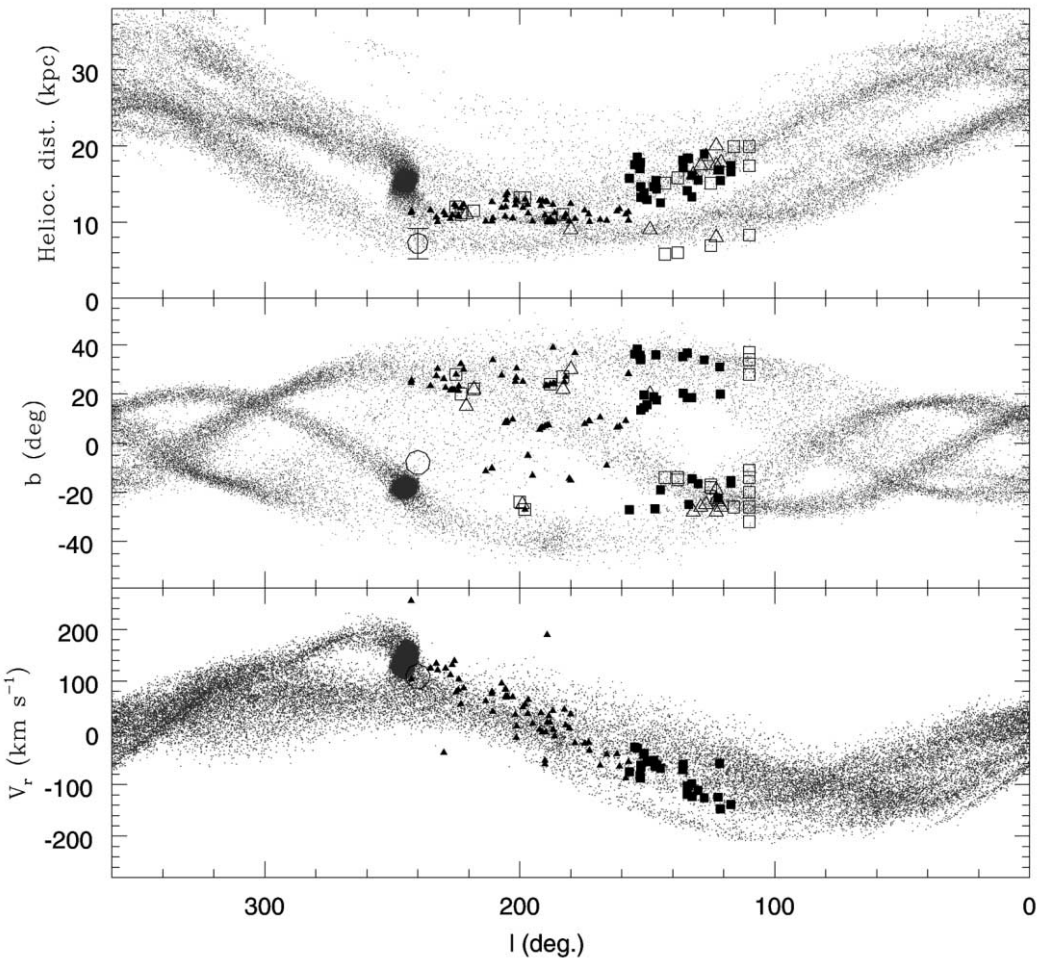

FIG. 8.—Comparison of our model for the Monoceros stream progenitor against CMa dwarf properties (*open circles*). *Top panel:* Heliocentric distances of stream particles from model *pro1* (*gray*) against observations. *Middle panel:* Projection in Galactic coordinates. *Bottom panel:* Heliocentric radial velocities.

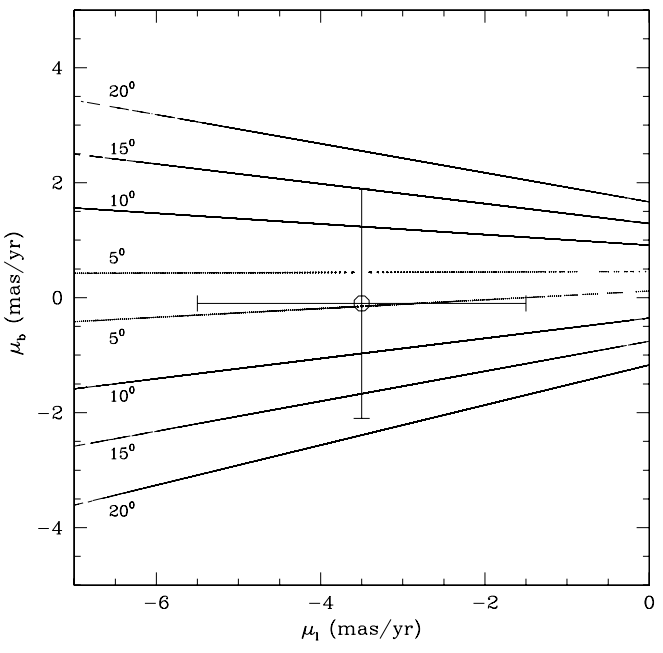

FIG. 9.—Orbital inclination of CMa as a function of μ_l, μ_b, fixing the radial velocity to 109 km s^{-1} and the heliocentric distance to $r_s = 7.2$ kpc.

that the value of i is strongly sensitive to the errors in proper motions. Taking into account the errors estimated by these authors, we obtain that, within 1 σ error, the orbital inclination of CMa lies in the range $i = [0^\circ,\ 18^\circ]$ if we fix the radial velocity to $v_r = 109$ km s^{-1} and the heliocentric distance to 7.2 kpc. Comparing this result with the best-fitting orbits that we present in this work, one can see the following:

1. The orbital eccentricity is fairly similar to the one we find (model *pro1* predicts $e = 0.10 \pm 0.05$).

2. The orbital inclination of CMa is too low to account for the large vertical dispersion of stream stars. This result is, however, not conclusive, since a orbit similar to that of model *pro1* lies within 1.5 σ error. More thorough measurements of proper motions are necessary to clarify the orbit of the CMa dwarf.

3. The geometrical and metallicity constrains that we can impose with the available observational data fix the final position of our best-fitting model at $l \simeq 245^\circ$, $b \simeq -15^\circ$ and a distance to the Sun of $r_s \simeq 15$ kpc. CMa appears in a direction similar to that of the main system of model *pro1*, but 7 kpc closer. If CMa proves to be the Monoceros stream progenitor, a way to reconcile the close distance of the CMa with the distant stream detections might be found by increasing the progenitor mass. A simple estimation of the decay rate induced by dynamical friction on nearly circular orbits is $\Delta r \propto M_s r \Delta t$ (eqs. [7]–[25] of Binney & Tremaine 1987). For model *pro1*, $\Delta r \simeq 3$ kpc after $\Delta t = 3$ Gyr. Imposing $\Delta r \simeq 9$ kpc in 3 Gyr leads to an initial mass of the

progenitor of approximately $M_s'/M_s = \Delta r'/\Delta r = 9/3 = 3$, i.e., $M_s' \simeq 1.8 \times 10^9\ M_\odot$. However, it is unclear whether the tidal debris of such a massive satellite would also reproduce the observed distribution. In order to check this assumption, new investigations adopting the CMa dwarf as the Monoceros stream progenitor appear necessary, which goes beyond the scope of this paper.

5.2.2. *Three-dimensional Velocity Distribution in the CMa Central Region*

We have also analyzed the distribution of radial velocities and proper motions in different regions of the stream in order to contrast them to the recently available observational values.

As we can observe in Figure 8, our model predicts a hot tail overlapping the progenitor remnants. This tail was stripped out approximately 0.6 Gyr ago and belong to the trailing tail (i.e., to the "inner ring"). In the top left panel of Figure 10 we plot the radial velocity distribution (*dotted line*) of 50 particles located in the neighborhood of the main system's projected position and compare it to that of the center of our satellite model (*solid line*; note that each distribution is separately normalized to the number of particles in the sample). This figure shows than the velocity distribution of both tails can be clearly differentiated, with peaks at $v_r \simeq 135$ km s^{-1} (cold tail) and $v_r \simeq 75$ km s^{-1} (hot tail). Although some particles of the underlying tail are included in the velocity distribution of the satellite center, one cannot identify a second peak because the surface density of the hot tail is much lower that of the satellite center. In the bottom left panel of this figure, we repeat the calculations in a crossing tail region, where the surface densities of both tails are comparable. In this case, one observes clearly two distributions of radial velocities (those from the distant and the close tail) in the same particle sample.

The observed low-dispersion bimodality cannot be reproduced by standard models of the Milky Way and is likely a proof of a stream detection, as we show here.

Intriguingly, Martin et al. (2004b) report a bimodal velocity distribution in CMa stars located at the center of the CMa dwarf. Measuring the radial velocity of 27 M-giant stars in 1° radius around CMa position, they observe two peaks in the radial velocity at $v_r \simeq 63$ km s^{-1} (10 stars) and $v_r \simeq 109$ km s^{-1} (17 stars), with very low dispersion (around 5 and 11 km s^{-1}, respectively). These values are around 20% larger than those of model *pro1*. Extrapolating the resulting distribution of our model to their detections suggests that in the CMa region two stream tails are overlapping. Moreover, the fact Martin et al. (2004b) measure similar number of stars in both peaks indicates that their surface density must be similar (if we assume that the number of M giants in a given stream is proportional to its surface density). This, however, contradicts the presence of a dwarf galaxy in Canis Major since the surface density at the center of these objects is several orders of magnitude larger than in the tidal streams.

That paradox might be solved if their small sample of M-giant stars were strongly contaminated with stars that belong to the hot tail surrounding CMa. In that case, the proper motions provided by these authors might be also affected. In right column of Figure 10 we show the distribution of proper motions in the regions indicated above. As in the distribution of radial velocities, different stream parts lead to well-differentiated curves. Looking at the region where the dwarf remnants are located, we can observe that the main system shows a fairly narrow distribution, with maxima at $(\langle \mu_l \rangle, \langle \mu_b \rangle) \simeq (-1.7, -0.6)$ mas yr^{-1}, whereas the distribution of the hot, overlapping stream tail is centered at $(\langle \mu_l \rangle,\ \langle \mu_b \rangle) \simeq (-3.4,\ 3.4)$ mas yr^{-1}. Therefore, including hot tail stars in the dwarf remnant sample (in a significant proportion) would lead to a smaller $\langle \mu_l \rangle$ and a larger $\langle \mu_b \rangle$, which results in a lower orbital inclination (see Fig. 9).

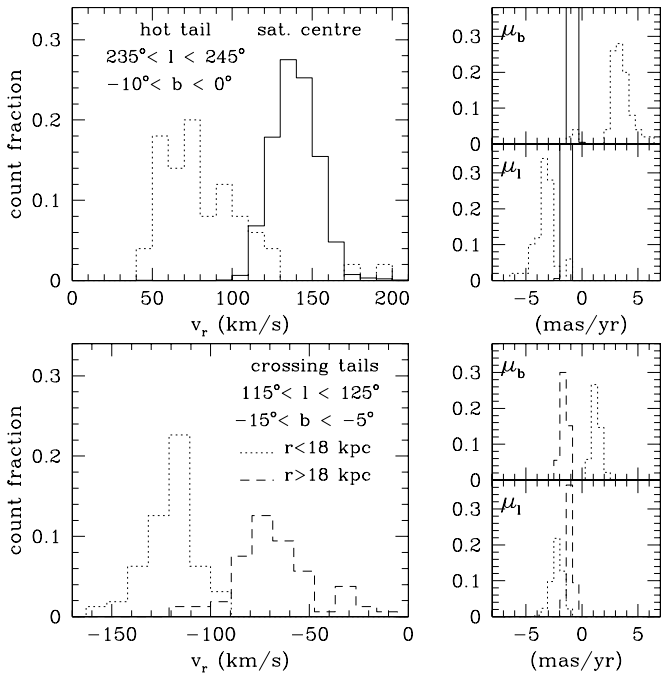

FIG. 10.—*Left panels:* Distribution of radial velocities in the CMa region from model *pro1* (*top*) and in a region of tail overlap (*bottom*). The velocity distribution of the satellite center includes particles within $243^\circ \leq l \leq 247^\circ$ and $-17 \leq b \leq -13^\circ$. The number of particles in each distribution was 8400 in the dwarf center and 50 in the surrounding tail. Dotted and dashed lines in the bottom panel show the distributions from particles in the inner and outer "rings," respectively. *Right panels:* Distribution of proper motions in the regions indicated above.

5.3. *Possible Associated Stellar Clusters*

Frinchaboy et al. (2004) have collected a set of 15 globular and open clusters that show a trend in their radial velocity curve, as well as in spatial location, which may indicate that those systems were stripped from a satellite in a disruption process.

Martin et al. (2004a) claimed that four of those clusters (NGC 1851, 1904, 2298, and 2808) belong to a globular cluster system associated with the CMa dwarf, arguing for the possible detection of the Monoceros stream's progenitor in Canis Major.

We have earlier shown that radial velocities and positions do not provide sufficient information to distinguish between pro- and retrograde orbital motions. In order to break that degeneracy, accurate measurements of proper motions are needed. In this section we test the possible association of those clusters with measured proper motions (NGC 1851, 1904, and 2298 from Dinescu et al. 1999) with the CMa dwarf. In addition, we also discuss the possible common origin of six "possibly associated clusters" suggested by Frinchaboy et al. (2004) by contrasting locations and radial velocities with the predictions of our best-fitting model. Unfortunately, no proper motions are available for those systems, so the results are not conclusive.

In Figure 11 we plot the *X*-*Y* projection of model *pro1* (*top panel*) and clusters listed to the right of the panel. In the bottom panel, the top plot shows the radial velocity, and the middle and bottom plots show the proper motions in the longitudinal (μ_l) and latitudinal (μ_b) directions, respectively. This figure shows the following with respect to CMa and other clusters:

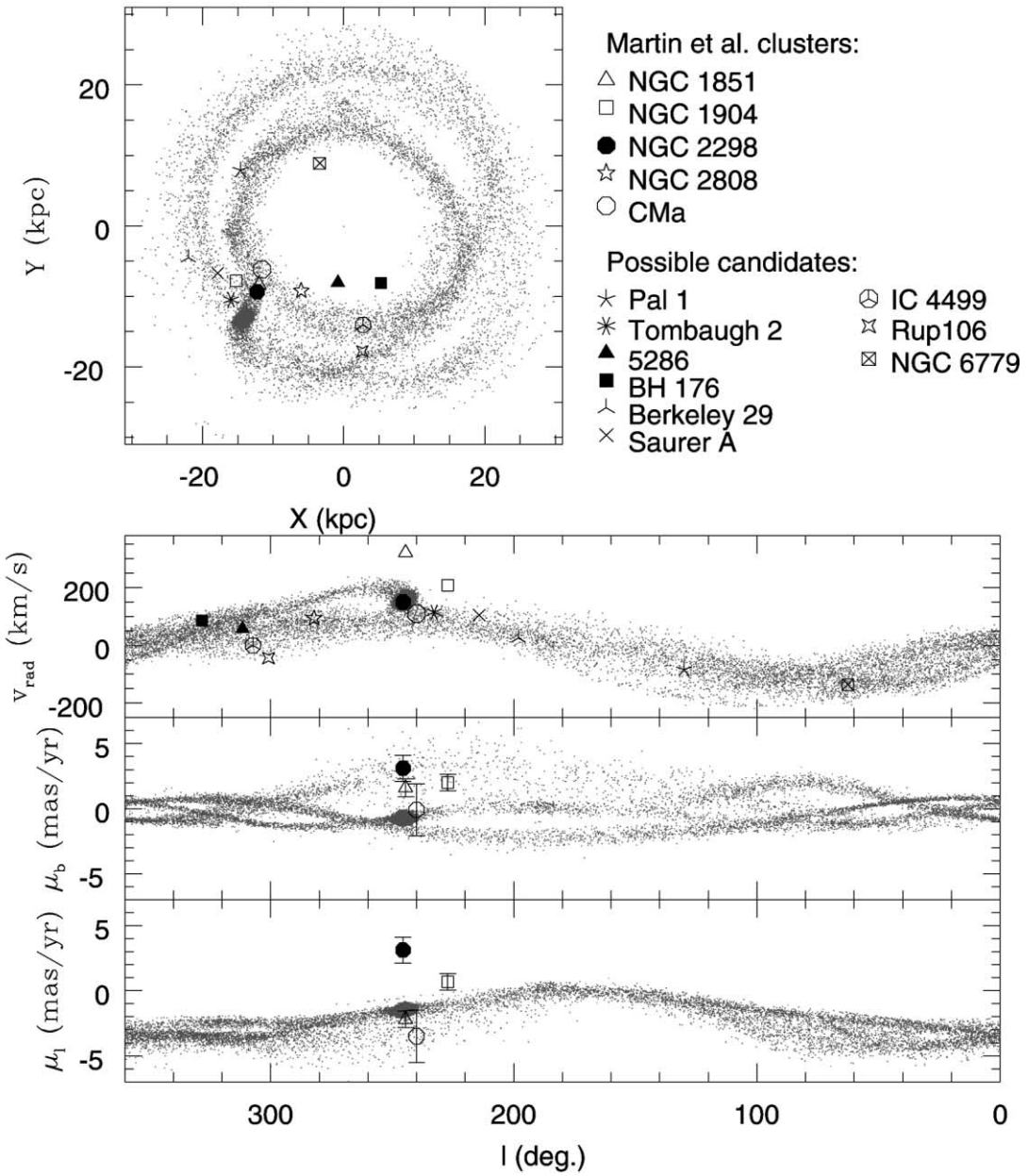

FIG. 11.—*Top panel: X-Y* projection of the model *pro1* debris against some globular and open clusters possibly associated with the Monoceros stream. *Bottom panel, top plot:* Radial velocity curve. *Bottom panel, middle plot:* Proper motions in the latitudinal component. *Bottom panel, bottom plot:* Proper motions in the longitudinal component. The open circle denotes the position and radial velocity of the CMa dwarf (Martin et al. 2004b).

CMa clusters.—None of these globular clusters present kinematical properties consistent with those of the CMa dwarf. First, NGC 1851 and NGC 1904 have radial velocities of approximately 320 and 208 km s^{-1}, whereas that of the CMa dwarf is approximately 109 km s^{-1} (Martin et al. 2004b). After integrating the orbit, we find that both globular clusters move on orbits with much higher eccentricities, $e = 0.7$ and $e = 0.65$, respectively (in agreement with Dinescu et al. 1999, who use a similar Galaxy potential). On the other hand, the orbital eccentricity of escaping particles remains fairly similar to that of the main body (see Fig. 5), leading to a well-defined radial velocity curve. If one assumes that this holds for stripped globular clusters, we come to the conclusion that NGC 1851 and 1904 are unlikely associated with CMa. In addition, the orbital inclinations of those systems are considerably higher than that of CMa.

The third globular cluster with measured proper motions, NGC 2298, follows a retrograde, highly eccentric orbit ($e \simeq 0.78$, Dinescu et al. 1999), arguing against any association with CMa and the other clusters.

Unfortunately, there are no proper motions available for NGC 2208, and therefore there is insufficient information to allow a determination of its possible association with CMa.

Other clusters.—In the middle plot of the bottom panel of Figure 11 we see that these clusters present a trend in radial velocities shown by Frinchaboy et al. (2004) consistent with our model. Their projected positions (*top panel*) also appear to form a "stream" in space. Searching through the Galactic globular cluster sample provides some additional, plausible candidates to be associated with the Monoceros stream: Rup 106, IC 4499, and NGC 6779, from a comparison of their projected position, distance, and radial velocity with the predictions of our model.

Unfortunately, whether or not these clusters are associated with the Monoceros stream cannot be asserted in the absence of proper motions.

5.4. *Thick-Disk Stars or Tidal Stream Debris?*

The main selection criteria used to discriminate between Milky Way stars and stars of an "external" origin were that (1) stream stars are observed to be in overdense regions not predicted by our standard Milky Way model and (2) the turn-off stars appear blue, old, and metal-poor, characteristics similar to those of the Sagittarius dwarf galaxy stars (Newberg et al. 2002). Those conditions by themselves do not exclude other explanations for the observations.

Here would like to comment briefly on two possible origins of the observed tidal streams: (1) thick disk and (2) a satellite disruption.

In § 4 we have shown that the stream detections can be reproduced by a disrupting satellite on a prograde, low-inclination, nearly circular orbit. The kinematical and as spatial distribution of debris resembles what one would expect for thick-disk stars (see Fig. 4) except for one point: it is difficult to reconcile the large vertical dispersion ($\Delta z = 2 \sin i \times 24.5$ kpc $\simeq 20$ kpc) and the large distances ($\sim$20 kpc from the Galaxy center) of proposed stream stars with a disklike distribution. To clarify this point, we have carried out a simple experiment: we have calculated the probability of finding thick-disk stars at the Monoceros stream location. The number of stars between m and $m + dm$, where m is apparent magnitude, can be written as

$$N(m)dm = N(r_s)\frac{dm}{dr_s}dr_s = N(r_s)\frac{5}{\ln 10}\frac{dr_s}{r_s}, \qquad (7)$$

where r_s is the distance of a star to the Sun. We have used the relationship $m - M = 5 \log_{10}(r_s)$ to convert distances into apparent magnitudes. The probability of finding a star between r_s and $r_s + dr_s$, in the range of solid angles $\Omega, \Omega + d\Omega$ is

$$N(r_s, \Omega)\, dr_s\, d\Omega = \rho(r_s, \Omega) r_s^2\, dr_s\, d\Omega, \qquad (8)$$

where $\rho(r_s, \Omega)$ is the thick-disk density distribution in the solar frame. Combining both equations, one has that the probability function is

$$P(r_s, \Omega) = A\rho(r_s, \Omega) r_s, \qquad (9)$$

where A is some normalization constant. The fraction of thick-disk stars in a given solid angle is therefore

$$N(r_s, \Omega) = \frac{\int_0^{r_s} \rho(x, \Omega)\, x\, dx}{\int_0^{\infty} \rho(x, \Omega)\, x\, dx}. \qquad (10)$$

As we can see, P is zero for $r_s = 0$ and $r_s \to \infty$, so that, for a given solid angle, there is a distance where the probability finds a maximum. In Figure 12 we plot the maximum likelihood isocontour of observing thick-disk stars (*thick solid line*) in the Galactic anticenter direction (eq. [9]). The Sun is placed at $R = z = 0$. Solid lines show the isocontours of the thick-disk fraction of particles as a function of their position in cylindrical coordinates when looking in the Galactic anticenter direction (eq. [10]). Dotted lines show the isocontours if looking 70° away (i.e., $l = 110°$ or $l = 250°$) in order to take into account the range of Galactic longitudes where the stream has been observed. In both cases we plot the 10%, 50%, and 90% contours. As we can see, the Galactic anticenter is the direction for which the number of distant thick-disk stars is maximum. For this plot, we have used the thick-disk model proposed by Chen et al. (2001), which follows exponential profiles in the planar and vertical directions with scale-lengths of 3.5 and 0.75 kpc, respectively.

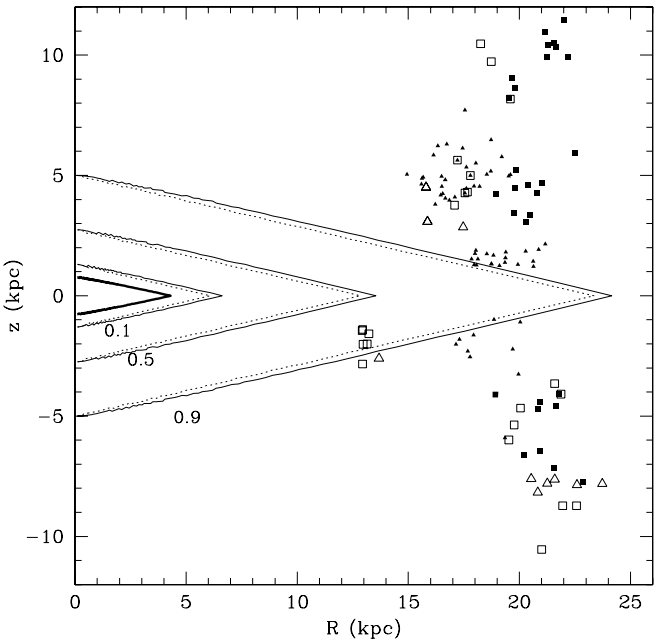

FIG. 12.—Isocontours of the thick-disk number of particles against stream detections. The Sun is located at $R = z = 0$. The strong line represents the maximum likelihood directions of finding thick-disk stars toward the Galactic anticenter ($l = 180°$). Lines show the R, z values where the number of thick-disk stars is 10%, 50%, and 90% of the total number if looking at the anticenter (*solid lines*) and 70° away (*dotted lines*).

This figure shows that stream detections presented in this work are unlikely related to the thick-disk population because (1) they are located in a narrow range of coplanar distances (R), as one would expect for debris from a disrupting galaxy in a nearly circular orbit; (2) they present a large vertical dispersion of approximately 20 kpc which cannot be reconciled with a disklike structure; and (3) they have been detected in positions where the fraction of thick-disk stars is $\leq$10% of the total number of stars in that direction. The only doubtful data might be found in the color-magnitude detections at $R \simeq 13$ kpc, which lie within 90% fraction of thick-disk stars. These points correspond to what our model identifies as the "close ring," which presents a higher metallicity than more distant detections.

It is interesting to note that stars stripped from the Monoceros stream progenitor have not yet contributed to the thick-disk population. The decay rate of the dwarf galaxy appears slower (around 3 kpc in 3 Gyr) than the mass-loss rate (50% in the same time period), so that the dwarf galaxy will be likely destroyed before reaching the inner regions of the thick disc. The mass-loss process, however, depends on the initial structural parameters of the dwarf, which were fixed ad hoc in this work. More accurate measurements of the stream surface brightness will provide better estimations of its survival time.

6. CONCLUSIONS

In this paper we have used a combined semianalytic N-body technique to explore the nature and origin of the Monoceros tidal stream. This method has allowed us to explore a large parameter space in a systematic way, with the goal of constraining the orbital properties of the Monoceros stream. We have found that the available observational data at the present day are sufficient to

robustly constrain some aspects of the Monoceros stream history and progenitor. In particular, (1) the heliocentric distance range at which the stream is observed plus the heliocentric radial velocity curve determines an orbital eccentricity of $e \simeq 0.10 \pm 0.05$, (2) the range of Galactic latitudes indicates an orbital inclination of $i \simeq 25^\circ \pm 5^\circ$ from the disk plane and, finally, (3) proper motions of stream stars are only compatible with a prograde orbit.

We found that it is considerably less straightforward to predict the main-body position through numerical calculations. The range of distances, the radial velocity curve, and the vertical extension of debris are relatively insensitive to the final location of the satellite galaxy, since they define a given volume in phase-space that the progenitor fills up after several wraps. Yet, the projected positions of stream tails are time-dependent, reflecting therefore the position of the main system, or equivalently, the final integration time of our *N*-body model.

Besides the uncertainty in the satellite remnant position, the lack of detections at low Galactic latitudes (owing to disk absorption within $b \in [-20^\circ,\ 20^\circ]$), as well as for a complete range of Galactic longitudes, makes it difficult to constrain the location of the main system. Owing to these limitations, our model matches the geometrical and kinematical distribution of debris if the main system remnants are located within the range $100^\circ \geq l \geq 200^\circ$, corresponding to integration times from 2.66 to 3.04 Gyr.

On the other hand, observations show that close detections of the stream have higher metallicities than the distant ones, which provides an additional constraint to our model. We have used this constraint by assuming that the progenitor's stellar metallicities are related to their initial binding energy. In particular, we assume that stars with low binding energies move, on average, in the outer satellite regions, and therefore should present lower metallicities than those with high binding energies. By comparing the initial binding energy (metallicity) distribution with observations for the range of locations commented above, we find that the metallicity gradient between the distant and the close detections can only be reproduced for integration times longer than 2.9 Gyr. In that case, the main system location ($l \sim 245^\circ$, $b \sim -18^\circ$) is similar to that of the CMa dwarf, with a heliocentric distance of 15.2 ± 0.8 kpc. The treatment employed to determine the distribution of metallicities in the stream is, however, approximate, because we have no way of knowing the initial metallicity gradient in the stream progenitor. Moreover, we implicitly assume that detections with different metallicities reflect an initial property of the progenitor. Other scenarios are possible, and, for example, we cannot rule out that streams with different metallicities at different distances belong to different progenitors.

The best-fitting model predicts a halo axis ratio of $q_h = 0.6$ (oblate). However, the poorly constrained selection function of observations and the incomplete area coverage leads to degenerated solutions for different values of q_h. In particular, we find that similar fits can be obtained with halo axis ratios $0.6 \leq q_h \leq 0.8$. These values appear in agreement with the result of Olling & Merrifield (2000), who estimate the density axis ratio of the Milky Way to be around 0.8 from kinematics of nearby stars. The Sagittarius tidal stream has also been used to constrain the shape of the Galaxy halo. In that case, however, the results are contradictory, and so whereas Ibata et al. (2001) estimate $q_h \sim 0.8$ to -0.9 from the stream width, Helmi (2004) shows that the recently obtained radial velocities along the stream can only be explained if the Milky Way halo is fairly prolate ($q_h \simeq 1.66$). Finally, Johnston et al. (2005) find that the actual Sagittarius stream precession is only consistent with an oblate Milky Way halo, $0.8 \leq q_h \leq 0.9$, ruling out the prolate case.

We must emphasize that the model presented here is far from being definitive. Future detections, mapping larger areas of the sky, will provide more constraints on the progenitor's orbit and a better determination of parameters listed in Table 3. New detections are also necessary to constrain the progenitor location by means of numerical models.

With the recently available kinematical data of the CMa dwarf, which Martin et al. (2004a) claim to be the progenitor of the Monoceros stream, we have integrated the orbit backward in time, comparing its orbital properties against those of our model. We find contradictory points in favor of and against that suggestion.

In favor:

1. The orbital eccentricity of CMa ($e \simeq 0.16$) and orbital sense of motion (prograde) are consistent with those of our model.
2. The projected location of CMa ($l = 240^\circ$, $b = -8^\circ$) is consistent with the geometrical and metallicity constraints imposed by the Monoceros stream stars.
3. The orbital inclination ($i \simeq 4^{+14}_{-4}$ deg) is consistent with that of our model within 1.5 σ errors from proper motions.
4. The radial velocity of CMa ($v_r = 109$ km s^{-1}) is also similar to that of our model ($v_r = 135$ km s^{-1}) and presents a low dispersion incompatible with thick-disk features.

Against:

1. The orbits of globular clusters NGC 1851, 1904, and 2298, which Bellazzini et al. (2004) and Martin et al. (2004a) claim to be an evidence that the CMa overdensity region is the remnant of the Monoceros stream progenitor, are inconsistent with the orbit of CMa, since NGC 1851 and NGC 1904 move on highly eccentric orbits and NGC 2298 on a retrograde, eccentric one.
2. The bimodality in the velocity distribution of CMa's M-giant stars (Martin et al. 2004b) can be reproduced by our model in regions where the projected positions of two stream tails overlap. That bimodality in v_r cannot be observed in the central part of our satellite model since the surface density is several orders of magnitude larger than that of overlapping stream tails. This fact seems to point to a possible contamination of background giant stars in the sample used to measure proper motions and the radial velocity of the main system. As a result, the orbital inclination might have been underestimated.
3. The main body of our best-fit model's progenitor is $\sim$15 kpc from the Sun—twice as distant as the observed CMa stellar structure. Since the mass of our model is poorly constrained, larger mass values cannot be rejected. In particular, dynamical friction would drive our satellite model down to 7.2 kpc in 3 Gyr for an initial mass of approximately $1.8 \times 10^9\ M_\odot$, whereas our best-fitting model has an approximate initial mass of $(6 \pm 3) \times 10^8\ M_\odot$. It remains unclear, however, whether the resulting distribution of debris from such a massive satellite undergoing tidal disruption would also reproduce the observations.

Unfortunately, with the results obtained in this work we cannot unambiguously determine whether the orbit of the CMa dwarf is consistent with that of the Monoceros stream progenitor, partly because of the uncertainty in the available observational data. Stricter criteria to select stars that belong to the CMa dwarf appear necessary to obtain reliable measurements of the kinematical properties of this system.

We want to thank Dana I. Dinescu for helping us to analyze the information obtained from proper motions. We also thank

H. Rocha-Pinto and J. D. Crane for giving us access to their data before it was published. Finally, we thank the anonymous referee for his/her useful comments on the paper.

Funding for the creation and distribution of the SDSS Archive has been provided by the Alfred P. Sloan Foundation, the Participating Institutions, the National Aeronautics and Space Administration, the National Science Foundation, the US Department of Energy, the Japanese Monbukagakusho, and the Max Planck Society. The SDSS Web site is (http://www .sdss.org).

The SDSS is managed by the Astrophysical Research Consortium (ARC) for the Participating Institutions. The Participating Institutions are the University of Chicago, Fermilab, the Institute for Advanced Study, the Japan Participation Group, Johns Hopkins University, Los Alamos National Laboratory, the Max-Planck-Institute for Astronomy (MPIA), the Max-Planck-Institute for Astrophysics (MPA), New Mexico State University, University of Pittsburgh, Princeton University, the United States Naval Observatory, and the University of Washington.

REFERENCES

Abazajian, K., et al. 2003, AJ, 126, 2081
Bellazzini, M., Ibata, R., Monaco, L., Martin, N., Irwin, M. J., & Lewis, G. F. 2004, MNRAS, 354, 1263
Binney, J., & Merrifield, M. 1998, Galactic Astronomy (Princeton: Princeton Univ. Press)
Binney, J., & Tremaine, S. 1987, Galactic Dynamics (Princeton: Princeton Univ. Press)
Boily, C. M., Kroupa, P., & Peñarrubia J. 2001, NewA, 6, 27
Chen, B., et al. 2001, ApJ, 553, 184
Crane, J. D., et al. 2003, ApJ, 594, L119
de Vaucouleurs, G. 1948, Ann. d'Astrophys., 11, 247
Dinescu, D. I., Girard, T. M., & van Altena, W. F. 1999, ApJ, 117, 1792
Fellhauer, M., Kroupa, P., Baumgardt, H., Bien, R., Boily, C. M., Spurzem, R., & Wassmer, N. 2000, NewA, 5, 305
Frinchaboy, P. M., et al. 2004, ApJ, 602, L21
Fukugita, M., Ichikawa, T., Gunn, J. E., Doi, M., Shimasaku, K., & Schneider, D. P. 1996, AJ, 111, 1748
Gunn, J. E., et al. 1998, AJ, 116, 3040
Harbeck, D., et al. 2001, AJ, 122, 3092
Helmi, A. 2004, ApJ, 610, L97
Helmi, A., Navarro, J. F., Meza, A., Steinmetz, M., & Eke, V. R. 2003, ApJ, 592, L25
Hernquist, L. 1990, ApJ, 356, 359
———. 1993, ApJS, 86, 389
Hogg, D. W., Finkbeiner, D. P., Schlegel, D. J., & Gunn, J. E. 2001, AJ, 122, 2129
Ibata, R., Gilmore, G., & Irwin, M. J. 1994, Nature, 370, 194
Ibata, R., Irwin, M. J., Lewis, G. F., Ferguson, A. M. N., & Tanvir, N. 2003, MNRAS, 340, L21
Ibata, R., Lewis, G. R., Geraint, F., Irwin, M., Totten, E., & Quinn, T. 2001, ApJ, 551, 294
Johnston, K., Law, D., & Majewski S. 2005, ApJ, 619, 800
Just, A., & Peñarrubia, J. 2005, A&A, 431, 861
King, I. R. 1966, AJ, 71, 65
Law, D. R., Johnston, K. V., & Majewski, S. R. 2005, ApJ, 619, 807
Majewski, S. R., Ostheimer, J. C., Rocha-Pinto, H. J., Patterson, R. J., Guhathakurta, P., & Reitzel, D. 2004, AJ, submitted (astro-ph/0406221)
Martin, N. F., Ibata, R. A., Bellazzini, M., Irwin, M. J., Lewis G. F., & Dehnen, W. 2004a, MNRAS, 348, 12
Martin, N. F., Ibata, R. A., Conn, B. C., Lewis, G. F., Bellazzini, M., Irwin, M. J., & McConnachie, A. W. 2004b, MNRAS, 355, L33
Martínez-Delgado, D., Butler, D., Rix, H. W., Franco, Y. I., & Penãrrubia, J. 2004, ApJ, submitted
Momany, Y., Zaggia, S. R., Bonifacio, P., Piotto, G., De Angeli, F., Bedin, L. R., & Carraro, G. 2004, A&A, 421, L29
Monet, D. G., et al. 2003, AJ, 125, 984
Munn, J. A., et al. 2004, AJ, 127, 3034
Navarro, J. 2004, preprint (astro-ph/0405497)
Newberg, H. J., et al. 2002, ApJ, 569, 245
Olling, R. P., & Merrifield, M.R. 2000, MNRAS, 311, 361
Pagel, B. E. J., & Edmunds, M.G. 1981, ARA&A, 19, 77
Peñarrubia J. 2003, Ph.D. thesis, Univ. Heidelberg
Peñarrubia, J., Just, A., & Kroupa, P. 2004, MNRAS, 349, 747
Peñarrubia, J., Kroupa, P., & Boily, C. M. 2002, MNRAS, 333, 779
Piatek, S., & Pryor, C. 1995, AJ, 109, 1071
Pier, J. R., Munn, J. A., Hindsley, R. B., Hennessy, G. S., Kent, S. M., Lupton, R. H., & Ivezic, Z. 2003, AJ, 125, 1559
Rocha-Pinto, H. J., Majewski, S. R., Skrutskie, M. F., & Crane, J. D. 2003, ApJ, 594, L115
Smith, J. A. et al. 2002, AJ, 123, 2121
Stoughton, C., et al. 2002, AJ, 123, 485
van den Bosch, F. C., Tormen, G., & Giocoli, C. 2004, MNRAS, submitted (astro-ph/0409201)
Wardle, J. F. C., & Kronenberg P. P. 1974, ApJ, 194, 249
Yanny, B., et al. 2003, ApJ, 588, 824
York, D. G., et al. 2000, AJ, 120, 1579